Nano Research

ISSN 1998-0124 CN 11-5974/O4
https://doi.org/10.26599/NR.2026.94909286

Research Article

Ultrathin and efficient wearable EMI shields with integrated self-powered sensing and information coding

Lingfeng Yu[1,2], Yanni Yang[3], Yihao Xiao[1,2], Song Luo[1], Shichun Hao[3], Jingzhe Yang[3], Qiang Chen[1], Lishun Fu[2](✉), Long Xia[3], Yahui Xue[1,4](✉)

[1] Department of Mechanics and Aerospace Engineering, and Center for Complex Flows and Soft Matter Research, Southern University of Science and Technology, Shenzhen 518055, China

[2] Shenzhen Key Laboratory of Transformation Optics and Spatial Modulation, Kuang-Chi Institute of Advanced Technology, Shenzhen 518057, China

[3] School of Materials Science and Engineering, Harbin Institute of Technology (Weihai), Weihai 264209, China

[4] Guangdong Provincial Key Laboratory of Sustainable Biomimetic Materials and Green Energy, Southern University of Science and Technology, Shenzhen 518055, China

Nano Res., **Just Accepted Manuscript** • https://doi.org/10.26599/NR.2026.94909286

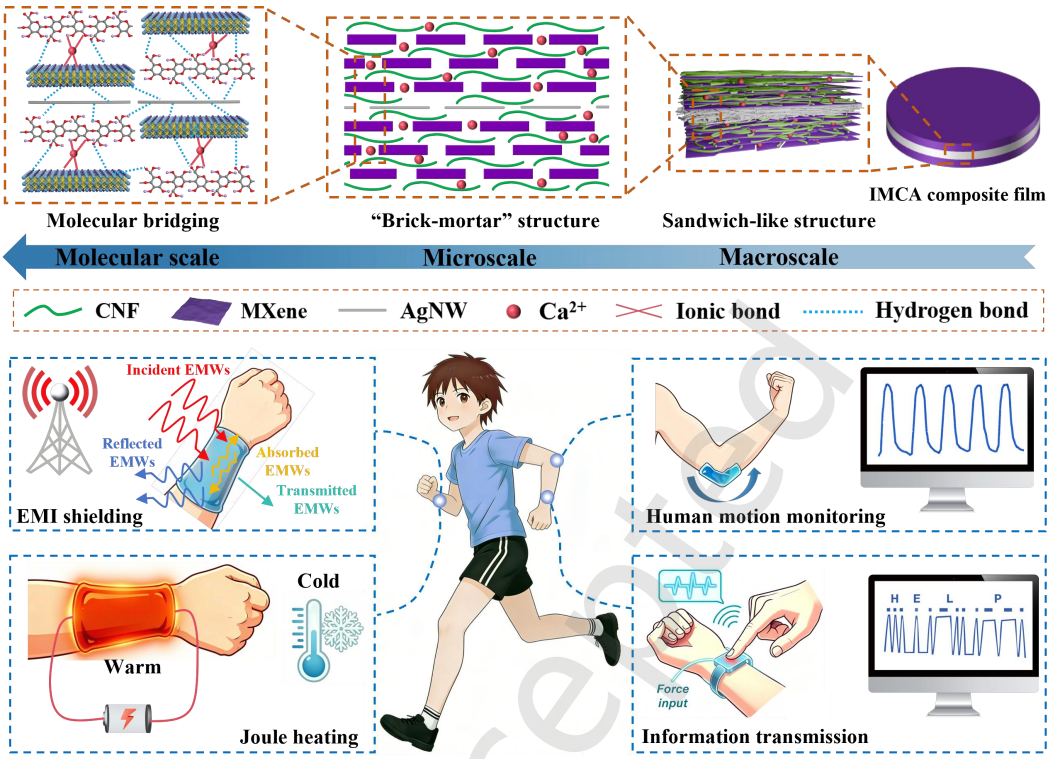
https://www.sciopen.com/journal/1998-0124 on Oct. 26, 2026

© The Authors(s)

Just Accepted

This is a "Just Accepted" manuscript, which has been examined by the peer-review process and has been accepted for publication. A "Just Accepted" manuscript is published online shortly after its acceptance,which is prior to technical editing and formatting and author proofing. Tsinghua University Press (TUP) provides "Just Accepted" as an optional and free service which allows authors to make their results available to the research community as soon as possible after acceptance. After a manuscript has been technically edited and formatted, and the page proofs have been corrected, it will be removed from the "Just Accepted" web site and published officially with volume and article number (e.g., *Nano Research*, **2025**, *18*, 94906990). Please note that technical editing may introduce minor changes to the manuscript text and/or graphics which may affect the content, and all legal disclaimers that apply to the journal pertain. In no event shall TUP be held responsible for errors or consequences arising from the use of any information contained in these "Just Accepted" manuscripts. To cite this anuscript please use its Digital Object Identifier (DOI®),which is identical for all formats of publication.

Graphical Abstract



This work demonstrates an ultrathin multiscale MXene/CNF-AgNW film featuring a hierarchical architecture that synergizes sandwich, nacre-like, and molecular-scale ionic bonding. It delivers exceptional mechanical robustness and ultrahigh EMI shielding, while serving as a self-powered E-skin for motion monitoring and information transmission. Integrated with machine learning, it enables 100% accurate handwriting recognition.

Just Accepted

Research Article

Ultrathin and efficient wearable EMI shields with integrated self-powered sensing and information coding

Lingfeng Yu[1,2], Yanni Yang[3], Yihao Xiao[1,2], Song Luo[1], Shichun Hao[3], Jingzhe Yang[3], Qiang Chen[1], Lishun Fu[2*], Long Xia[3], Yahui Xue[1,4*]

[1] Department of Mechanics and Aerospace Engineering, and Center for Complex Flows and Soft Matter Research, Southern University of Science and Technology, Shenzhen 518055, China

[2] Shenzhen Key Laboratory of Transformation Optics and Spatial Modulation, Kuang-Chi Institute of Advanced Technology, Shenzhen 518057, China

[3] School of Materials Science and Engineering, Harbin Institute of Technology (Weihai), Weihai 264209, China

[4] Guangdong Provincial Key Laboratory of Sustainable Biomimetic Materials and Green Energy, Southern University of Science and Technology, Shenzhen 518055, China

Received: 13 August 2026; **Revised:** 28 September 2026; **Accepted:** 26 October 2026

Address correspondence to Yahui Xue, xueyh@sustech.edu.cn; Lishun Fu, lishun.fu@kuang-chi.com

Cite this article: *Nano Research*, 2026, 19, 94909286 https://doi.org/10.26599/NR.2026.94909286

Just Accepted

Abstract

Developing ultrathin and robust high-performance electromagnetic interference (EMI) shielding materials with multifunctional integration for wearable electronics is imperative yet remains challenging. Here, we report a bioinspired versatile and wearable MXene/cellulose nanofiber-silver nanowire (MXene/CNF-AgNW) composite film with superior mechanical strength, high-efficiency EMI shielding and integrated self-powered sensing capabilities. The film achieves superior mechanical robustness with a high tensile strength reaching 315 MPa through a multiscale reinforcement strategy that combines hybrid sandwich and nacre-like structures. The sandwiched AgNWs with MXene/CNF-based shells impart the composite film with high electrical conductivity and excellent EMI shielding effectiveness (EMI SE) reaching 62 dB for a tiny thickness of 23 μm, corresponding to an outstanding specific EMI SE (SSE/t) of 16550 $dB \cdot cm^2 \cdot g^{-1}$, together with remarkable electrothermal conversion capability. Furthermore, the flexible and

antibacterial film can also serve as wearable electronic skin with self-powered sensing for human activity monitoring and information coding. Notably, by integrating a machine learning algorithm, the system can enable intelligent handwriting recognition with an accuracy of 100%, establishing an advanced communication interface. This work provides a facile multiscale engineering strategy for constructing multifunctional composite films that seamlessly integrate protection, perception, and communication functionalities for next-generation smart wearable electronic applications.

Keywords: electromagnetic interference (EMI) shielding; hierarchical structure; mechanical robustness; self-powered sensing; wearable electronic skin

1. Introduction

With the advent of the artificial intelligence era and the popularization of the Internet of Things (IoT), the implementation of highly integrated electronic devices has led to severe electromagnetic radiation pollution. It not only impacts the operational stability of precision equipment, precipitates irreversible malfunctions but also endangers public health [1-8]. Therefore, it is extremely desirable to develop electromagnetic interference (EMI) shielding materials to mitigate electromagnetic pollution. Particularly, high-performance EMI shielding films should feature light weight, reduced thickness and superior mechanical properties to satisfy the demands of modern wearable electronics [9-11]. To further accommodate the diversity of application scenarios, the advanced EMI shielding composite films also benefit from the integration of additional functionalities such as thermoregulation and perception for smart and wearable electronics [12,13]. Thus, it is imperative to develop versatile and mechanically robust composite films with exceptional EMI shielding performance and multifunctional integration.

High electrical conductivity is desirable for enhanced shielding effectiveness (SE) of EMI shielding materials [14,15]. Recently novel conductive nanomaterials, such as graphene, carbon nanotube (CNT), silver nanowire (AgNW) and MXene, have attracted great attention for EMI shielding application [16-23]. Among them, the one-dimensional AgNW features facile preparation, large aspect ratio and prominent electrical conductivity, and has been widely used in composite films, foams, and aerogels for efficient EMI shielding [24-27]. Moreover, the release of free silver ions (Ag^+) from AgNWs enables the elimination of surrounding microbial bacteria, thereby imparting the EMI shielding material with additional antibacterial functionality [28]. However, independent AgNWs do not easily form strong films and are commonly mixed with

Just Accepted

polymers to construct a homogeneous structure for enhanced mechanical performance [29-31]. The introduction of insulating polymers into the conductive network of AgNWs inevitably compromises the overall electrical conductivity and thereby degrades the EMI shielding performance, indicating a typical trade-off between mechanical properties and EMI SE. For instance, a homogeneously structured AgNW/carboxymethyl cellulose nanofiber (AgNW/CMC) film has been fabricated and shows an EMI SE of 32 dB and a tensile strength of 45 MPa [31]. A multilayered structure has been used to boost the mechanical and EMI shielding performance of aramid nanofiber/silver nanowire (ANF/AgNW) film that displays a tensile strength of 79 MPa and an EMI SE of 63 dB [32]. It is therefore evident that the synergetic optimization of the mechanical and EMI shielding performance of composite films still remains a significant challenge.

Nature offers an elegant blueprint for enhancing the mechanical performance of composite films through the nacreous "brick-and-mortar" architecture, wherein rigid inorganic platelets are bridged by tough organic matrices, delivering exceptional mechanical strength and toughness simultaneously [33-35]. Biomimetic composites assembled from MXene "bricks" with cellulose nanofiber (CNF) "mortar" via hydrogen bonds have demonstrated improved mechanical performance [36-38]. In addition, further mechanical property enhancement can be achieved via the incorporation of ionic crosslinking at the molecular level [39-42]. Nevertheless, it still requires further optimization of the multiscale architectures with no compromise on the electrical conductivity to achieve simultaneously high EMI SE as well.

Beyond achieving synergistic mechanical and shielding performance, the development of intelligent wearable EMI shields demands a paradigm shift from passive EMI shielding materials toward multifunctional platforms that harmoniously integrate shielding protection, sensory perception and information transmission. Triboelectric-based self-powered sensing, which harvests biomechanical energy from joint motion or touch to eliminate the energy bottleneck of miniaturized wearables has enabled applications ranging from human activity monitoring to Morse code-based emergency communication [43-46]. Notably, coupling these platforms with machine learning algorithms can further support high-fidelity recognition for advanced human-machine interfaces [47]. Despite these advances, it remains elusive to seamlessly converge EMI shielding, sensing and information communication within a single platform.

Just Accepted

In this work, we present an ionic-crosslinked MXene/CNF-AgNW (IMCA) composite film with a hierarchical architecture that integrates the sandwich and nacre-like structures with molecular‑ scale bridging for multiscale reinforcement. The whole architecture can be feasibly achieved by a sequential process involving vacuum-assisted filtration, ionic crosslinking, and hot-pressing. The obtained film exhibits a superior tensile strength approaching 315 MPa, alongside excellent electrical conductivity enabled by the sandwiched AgNW conductive network. As a result, the 23-μm-thick film achieves an exceptional EMI SE of 62 dB, with a specific EMI SE (SSE/t) as high as 16550 $dB \cdot cm^2 \cdot g^{-1}$. The film also demonstrates efficient thermoregulation and antibacterial properties, making it suitable as self-powered electronic skin for human motion sensing and information coding and transmission. Moreover, the integration of a machine learning algorithm enables handwriting recognition with an accuracy of 100%, providing an intelligent communication interface. This work establishes a universal and scalable paradigm for fabricating mechanically robust composite films tailored to next-generation wearable electronics, which seamlessly merge the core functionalities of shielding protection, sensory perception, and information communication.

2. Experimental section

2.1. Materials

Lithium fluoride (LiF, AR), ethylene glycol (EG, AR), calcium chloride ($CaCl_2$, AR), silver nitrate ($AgNO_3$, AR), hydrochloric acid (HCl, AR) and poly(vinylpyrrolidone) (PVP, AR) were purchased from Sinopharm Chemical Reagent Co., Ltd. Ti_3AlC_2 powder (purity > 98.0%, 400 mesh) was supplied by Jinan Sanchuan New Materials Technology Co., Ltd. Polydimethylsiloxane (PDMS) and its curing agent were bought from Dow Corning Co., Ltd. Cellulose nanofiber (CNF) aqueous dispersion (1.05 wt.%) was obtained from Tianjin Woodelf Biotechnology Co., Ltd.

2.2. Fabrication of the composite films

The synthesis of MXene and AgNW suspensions is described in Supplementary Information. The IMCA composite films were fabricated through a sequential vacuum-assisted filtration and ionic crosslinking method. First, a certain amount of MXene suspension and CNF suspension were mixed at a mass ratio of 1:1, and the mixture was then ultrasonically stirred to achieve a homogeneous mixture. The above uniform dispersion was subjected to vacuum-assisted filtration through a filter membrane to yield a stable MXene/CNF hydrogel. Afterwards, the desired AgNW

Just Accepted

aqueous dispersion was deposited on the surface of the MXene/CNF hydrogel using the same method. Next, the same total weight and mass ratio of MXene/CNF uniform dispersion was sedimented onto the surface of the AgNW layer. Then, the obtained wet composite film underwent overnight drying at ambient temperature, followed by being peeled from the filter membrane upon full dehydration. Finally, the composite film was soaked in an appropriate volume of $CaCl_2$ solution (20 mg/mL) for 12 h, then rinsed with distilled water and was hot-pressed at 25 MPa and 80 ℃ for 30 min. The final composite films were denoted as IMCA-X (X=0, 2.5, 5, 10 and 15), where X represents the mass fraction of AgNW with respect to the total mass of the composite film. For comparison, composite films were prepared by the identical process except for the absence of ionic crosslinking and the series of composite films was labeled as MCA-Y (Y=0, 2.5, 5, 10 and 15). In addition, CNF, MXene/CNF and MXene/CNF with ionic crosslinking (I-MXene/CNF) films were prepared as well for comparison.

2.3. Characterizations and measurements

The crystal structures of the samples were investigated by an Rigaku SmartLab X-ray diffractometer (XRD) using Cu Kα radiation (λ = 1.5418 Å), with a scanning rate of 5°/min. Morphological and microstructural analyses of the samples were conducted using a Zeiss Merlin scanning electron microscope (SEM), an FEI Talos F200x transmission electron microscope (TEM), and a Cypher ES atomic force microscope (AFM). Intermolecular interactions were determined on a Vertex-70 Fourier transform infrared (FT-IR) spectrometer and a Thermo Scientific K-Alpha X-ray photoelectron spectrometer (XPS). The electrical conductivity of the samples was determined using an RTS-9 four-probe tester. Tensile testing was conducted on a SANS CMT4014 universal testing machine at a tensile speed of 1 mm/min and further details are provided in Note S3 of Supplementary Information. The EMI shielding performance of the film was evaluated using a Ceyear 3671D vector network analyzer via the waveguide method in the X-band (see Note S3 of Supplementary Information for details). The tests for EMI shielding durability, Joule heating, sensing, and antibacterial properties are detailed in Note S3 of Supplementary Information.

3. Results and discussion

3.1. Structural design and characterizations of the IMCA film

The preparation of the versatile IMCA composite film reinforced with multiscale structures is

Just Accepted

schematically illustrated in Fig. 1a. The fabrication process integrates successive vacuum-assisted filtration with structural engineering to combine multiple functional components for enhanced mechanical properties. First, MXene/CNF, AgNW and MXene/CNF were deposited sequentially on the filter membrane to create a sandwich-like composite film, and then the film was immersed in a $CaCl_2$ aqueous solution for ionic crosslinking, and the resultant film was finally hot-pressed for sequential performance tests. As depicted in Fig. 1b, the IMCA composite film exhibits a sophisticated multiscale architecture that synergistically integrates macroscale, microscale and molecular-scale reinforcement for superior mechanical properties. At the macroscale, the film adopts a sandwich-like structure. At the microscale, the film features an intricate nacre-like "brick-mortar" architecture. At the molecular scale, hydrogen bonds enhance interfacial interactions, and the incorporation of Ca^{2+} ions induces the formation of robust ionic bridging. The as-prepared IMCA film demonstrates multifunctionality such as EMI shielding, Joule heating, self-powered human motion monitoring and information transmission (Fig. 1c), highlighting its potential as a versatile platform for next-generation wearable electronics.

The AgNWs used here were synthesized by the solvothermal method (Note S1). The obtained AgNWs exhibit uniform fiber structures with high aspect ratio (Fig. S1a). The XRD pattern (Fig. S1b) reveals the crystal structure of the AgNWs. It exhibits five typical characteristic diffraction peaks at 2θ of 38.2°, 44.4°, 64.61°, 77.6° and 81.8°, attributed to the (111), (200), (220), (311) and (222) crystal planes of silver, respectively (JCPDS no. 04-0783) [48], confirming the successful preparation of AgNWs. Fig. S2 shows the TEM image of AgNWs, revealing an ultrathin PVP layer on the surface. The PVP layer acts as a protective barrier, preventing the AgNWs from being easily oxidized. More importantly, the functional groups of PVP facilitate the formation of intermolecular interactions [49]. The observed lattice spacing of 0.123 nm is assigned to the (311) plane of silver (Fig. S2), which is in good agreement with the above XRD result. The HAADF-STEM and element mapping (Fig. S3) reveal that Ag constitutes the majority of AgNWs, which imparts exceptional conductivity and Joule heating properties.

The MXene nanosheets were synthesized by selective etching in the HCl-LiF system and ultrasonic exfoliation of MAX precursor (Note S2 and Fig. S4). The peak at 39° has essentially vanished and the (002) peak shifts from 9.54° to 7.05° (Fig. S5), demonstrating the successful elimination of the Al layer from MAX. The finally obtained MXene nanosheet dispersion shows

Just Accepted

excellent hydrophilicity and dispersibility, which is manifested by the obvious Tyndall effect (Fig. S6). Moreover, the MXene nanosheet exhibits a thickness of 1.31 nm (Fig. S7), which aligns well with the characteristics expected for a monolayer MXene nanosheet [50]. The MXene nanosheets present micron-sized lateral dimensions, demonstrating a sheet-like structure (Fig. 2a). A uniform distribution of elements C, Ti, and O in MXene is confirmed by EDS mapping (Fig. S8). The CNFs exhibit a large aspect ratio, making them suitable for serving as the soft mortar in the nacre-like structure (Fig. S9).

The mixing of MXene with CNF induces the (002) peak of the XRD patterns being shifted from 7.05° to 5.95°, indicating a uniform interlayer structure with relatively increased spacing (Fig. 2b). Fig. 2c illustrates the XRD patterns for a series of IMCA-X films. With the increase in the AgNW amount, the films display increasingly intense diffraction peaks at 2θ of 38.8° and 44.3°, assigned to the (111) and (200) crystal planes of silver. FT-IR and XPS analyses were carried out to elucidate the chemical structures and interactions among AgNW, CNF and MXene. Fig. 2d presents the FT-IR spectra of CNF, AgNW, and CNF/AgNW films, respectively. Notably, CNF exhibits a typical peak at 3330 cm^{-1}, attributed to the stretching vibration of the hydroxyl group (-OH). Concurrently, a distinct peak observed at 1637 cm^{-1} corresponds to the stretching vibration of the carbonyl group (C=O) on the surface of AgNW derived from PVP [48]. It is important to highlight that in comparison with the FT-IR spectra of CNF and AgNW, the -OH peak and C=O peak in the spectrum of CNF/AgNW shift from 3330 cm^{-1} to 3317 cm^{-1} and from 1637 cm^{-1} to 1621 cm^{-1}, respectively. This red shift means that hydrogen bonding interactions are formed between the -OH groups of CNF and C=O groups of AgNWs. Similarly, the MXene displays a prominent absorption peak at 3498 cm^{-1} (Fig. 2e), corresponding to the -OH bond. Notably, for the CNF/MXene film, the absorption peak for the -OH shifts to 3368 cm^{-1}, indicating the establishment of significant hydrogen bonding interactions between CNF and MXene [51]. In addition, as illustrated in Fig. 2f, the C=O shifts from 287.7 eV to 288.1 eV. Fig. 2h shows that a new peak at 281.3 eV corresponding to C-Ti is found in CNF/MXene due to the introduction of MXene. Furthermore, the C=O shifts from 288.1 eV to 287.8 eV. This altered chemical environment of the C=O further confirms the formation of hydrogen bonds. As shown in Fig. S10 and Fig. 2h, XPS spectra show that the IMCA-10 film has a new peak for Ca consisting of Ca $2p_{1/2}$ (351.38 eV) and Ca $2p_{3/2}$ (347.88 eV), proving the ionic crosslinking modification.

Just Accepted

The obtained film presents a very smooth and flat surface (Fig. 2i and Fig. S11a). The uniform distribution of the surface Ti, C and Ca elements (Fig. S11b) implies the homogeneous structure of the MXene/CNF mixture after ionic crosslinking. The three-layered sandwich structure of the IMCA-10 composite film can be easily distinguished (Fig. 2j): the upper and bottom MXene/CNF, and middle AgNW layers. The MXene/CNF layer acting as the shell exhibits a nacre-like "brick and mortar" structure (Figs. 2k and l), facilitating the improvement of the mechanical performance. The independent AgNW layer located in the middle consists of a continuous conductive network and serves as the primary shielding layer. Fig. 2m shows the cross-sectional SEM image and EDS mapping image of the IMCA-10 composite film. The film demonstrates a compact layered structure with no observable delamination, suggesting strong bond strength between successive layers. The elemental mapping images unveil that Ti, C and Ca elements are primarily distributed in the upper and lower layers, whereas the Ag element is predominantly concentrated in the middle layer, which confirms the successful development of a composite film with a sandwich-like structure. Such hybrid sandwich and nacre-like structures are expected to achieve improved mechanical properties and EMI shielding performance.

3.2. Mechanical properties of the films

We investigate the mechanical properties of the IMCA films and the dependence on the constitutive compositions. Figs. 3a and b display the tensile stress-strain curves and mechanical strength of CNF, MXene/CNF and I-MXene/CNF films. The pristine CNF film exhibits a tensile strength of 146 MPa. The incorporation of 2D MXene nanosheets into the CNF framework results in a considerable enhancement in tensile strength to 199 MPa, ascribed to the nacre-like "brick-mortar" structure and strong hydrogen bonding interactions. Moreover, the mechanical strength of the MXene/CNF film is further improved to 255 MPa through ionic crosslinking. These highly robust composite films serve as shells to sandwich the independent AgNW layer, thereby enabling the realization of high-strength AgNW-based EMI shielding composite film.

We also probe the tensile performance of the MCA-Y films prior to ionic crosslinking (Fig. S12). It is seen that, with the increase in the AgNWs content, the tensile strength of the films increases first and then decreases. When the AgNWs content is 10 wt.%, the MCA-10 film achieves the highest tensile strength of 246 MPa, ascribed to the sandwich-like structure and strong hydrogen bonding interactions within the whole film. When the AgNWs content further

Just Accepted

increases to 15 wt.%, the corresponding tensile strength drops due to the weakened adhesion between the MXene/CNF and AgNW layers.

We observe the mechanical properties of the IMCA-X films are further improved after the MCA-Y films undergo ionic crosslinking, as shown in Figs. 3c and d. Specifically, the tensile strength of the IMCA-10 film can reach as high as 315 MPa, and such impressive mechanical property is attributed to the multiscale synergistic effect resulting from the hybrid sandwich and nacre-like structure, extensive interfacial hydrogen bonding and ionic bridging (Fig. 1a). The IMCA-10 film can easily lift a 400 g weight without breakage, demonstrating its exceptional mechanical robustness (Fig. S13). Further increasing the AgNWs content beyond 10 wt.% leads to reduced tensile strength, consistent with the observation in Fig. S12b. Even at an AgNW content of 15 wt.%, the IMCA-15 film still possesses a high tensile strength of 240 MPa. To shed light on the underlying fracture mechanism, we investigate the morphology of tensile fracture surface of the IMCA-10 film (Figs. 3e-h). Figs. 3e and f reveal the hierarchical fracture surface along the stretching direction. The closely packed lamellar structure of the IMCA-10 film remains largely intact following the tensile test (Fig. S14). The existence of "zigzag" cracks is evidenced in IMCA-10 film (Figs. 3g and h), which indicates a discrete and progressive cracking process. During initial stretching, interfacial sliding initially occurs at the AgNW-AgNW interface due to its weaker interfacial bonding. Upon further stretching, AgNWs slide further and the hydrogen bonds between AgNW and MXene/CNF gradually begin to break, increasing energy dissipation. Concurrently, MXene nanosheets also begin to slide past each other. As the tensile load increases, the coiled CNF molecular chains gradually extend to create sufficient slip space for the MXene nanosheets. During this period, the hydrogen bonds and ionic bonds between the CNF molecules and MXene nanosheets continuously rupture and reform to dissipate energy. As stretching continues, the CNF molecular chains become fully extended, resulting in complete disruption of the hydrogen and ionic bonds, which improves energy dissipation and contributes to enhanced tensile strength. Such multiple interfacial interactions facilitate stress transfer and energy dissipation during the crack propagation process. The multiple strong interfacial interactions throughout the process thereby synergistically augment the stress-transfer efficiency and facilitate substantial energy dissipation, as schematically shown in Fig. 3i. Furthermore, the IMCA-10 film can be bent, folded and rolled, confirming its excellent flexibility and robustness (Fig. 3j).

Just Accepted

3.3. EMI shielding performance of the films

We first examine the electrical conductivity of the IMCA films that is highly correlated with EMI shielding performance [21]. As shown in Fig. 4a, these films display excellent electrical conductivity, and their electrical conductivity progressively rises as the AgNW content increases. A high electrical conductivity of 960 $S \cdot cm^{-1}$ is achieved at an AgNW content of 15 wt.%, indicating the film can be used as an effective EMI shielding material. As presented in Fig. 4b, the IMCA-0 film has the lowest EMI SE of 26.4 dB, exceeding the commercial standard (20 dB) [9]. However, when AgNWs are introduced, the EMI shielding performance increases sharply. When the AgNWs content is 2.5 wt.%, the IMCA-2.5 film exhibits an enhanced EMI SE of 47.4 dB. As the content of AgNWs reaches 10 wt.%, the EMI SE of 62 dB can be achieved, originating from the continuous conductive network established by closely arranged AgNWs, far surpassing the commercial requirements for EMI shielding. When the AgNW content is 15 wt.%, the EMI SE is up to 66 dB. As shown in Fig. 4c, both SE_A and SE_R show an upward trend with enhanced electrical conductivity, which aligns with the variation of SE_T. The increase in SE_R is attributed to the progressive development of the conductive network with increasing AgNW content, which leads to an increasingly severe impedance mismatch between the film and air. Meanwhile, the well-developed conductive network significantly enhances the ohmic loss, thereby promoting the dissipation of electromagnetic waves (EMWs), i.e., an increase in SE_A. To analyze the EMI shielding mechanism, we calculated the power coefficients (A, R and T). As the AgNW content increases, a decrease in the T value indicates a reduction in the EMWs transmitted through the film and the R value presents an increasing trend approaching 0.99, and consistently remains higher than the A value (Fig. 4d), implying that the IMCA-X composite films have a reflection-dominated shielding mechanism.

To better emphasize the EMI shielding capability of the films, we assess the SE/t and SSE/t, which respectively represent SE per unit thickness and specific SE per unit thickness. As illustrated in Fig. 4e, the SSE/t value of the IMCA-10 film with an ultra-low thickness of 23 μm reaches an impressive 16550 $dB \cdot cm^2 \cdot g^{-1}$. When compared to existing literature on EMI shielding materials derived from metals, MXene, and carbon-based substances, the SSE/t value for the IMCA-10 film in this work ranks among the highest (see Fig. 4e and Table S1). Moreover, the IMCA-10 film simultaneously achieves an exceptional tensile strength of 315 MPa and a high

Just Accepted

SE/t of 26956 $dB \cdot cm^{-1}$, outperforming most previously reported composite films (see Fig. 4f and Table S2).

We further demonstrate the durability of the IMCA films for EMI shielding applications in extremely harsh conditions. A series of tests, including ultrasonication, tape stripping and chemical solvent soaking, are carried out. The film is ultrasonicated for 1 h, subjected to 100 tape stripping cycles, and treated with a chemical solvent for 24 h. The resultant IMCA-10 film still demonstrates high EMI SE retention above 95% (Fig. S15). Even after exposure to ambient oxidation and damp heat aging, the film maintains a high EMI SE (Fig. S16). Moreover, the EMI SE of the film exhibits negligible deterioration following 400 bending cycles, confirming its superior mechanical durability (Fig. S17). This exceptional durability implies that the protective MXene/CNF layers, coupled with strong interfacial interactions, endow the composite with a robust architecture essential for durable EMI shielding applications.

We used the Tesla coil experiment to visually demonstrate the EMI SE of the IMCA-10 film (Fig. 4g). When the power switch is activated, the LED light remains illuminated. In contrast, the pure CNF film fails to turn off the LED lamp. However, when the IMCA-10 film is positioned between the LED light and the Tesla coil, the LED light goes off. This is attributed to the disruption of resonance conditions within the Tesla coil system caused by the introduction of the IMCA-10 film. In addition, the EMI shielding effect of the IMCA-10 film is also evaluated by the interference to the wireless charging to smartphones. By inserting a CNF film between the smartphone and the wireless charger, the charging is not affected, but when the CNF film is replaced with the IMCA-10 film of the same thickness, the charging is immediately stopped (Fig. 4h and Fig. S18). This clearly demonstrates that the IMCA-10 film can effectively block wireless power transmission.

A schematic illustration of the underlying EMI shielding mechanism of the IMCA-10 film is presented in Fig. 4i. Upon incidence, a significant portion of EMWs is directly reflected at the air/MXene/CNF interface due to the severe impedance mismatch between the conductive outer layer and free space [10]. The residual EMWs that penetrate into the film interior are subsequently partially absorbed. Within the film, multiple internal reflections and interface polarization arise from the abundant heterogeneous interfaces between highly conductive MXene nanosheets and CNFs, further amplifying electromagnetic energy loss and promoting the attenuation and

Just Accepted

conversion of EMWs into heat. Additionally, the high electrical conductivity of the MXene nanosheets facilitates ohmic loss, in which mobile charge carriers interact with the electromagnetic field to dissipate energy as heat. Moreover, defects and oxygen-containing functional groups on the MXene nanosheets induce an asymmetric charge distribution, generating local dipoles that undergo dipole polarization under an alternating electromagnetic field [17]. Upon reaching the highly conductive AgNW interlayer, the EMWs encounter another impedance mismatch and are reflected back toward the MXene/CNF layers, thereby contributing to further attenuation. Simultaneously, the continuous conductive network formed by the interconnected AgNWs significantly reduces the sheet resistance, enabling a greater number of mobile charge carriers to interact with the incident EMWs, which results in substantial ohmic loss and further dissipates electromagnetic energy [26]. Furthermore, the distinctly different dielectric properties at the upper and lower MXene/CNF-AgNW interfaces result in interfacial charge accumulation, inducing interfacial polarization to enhance EMWs attenuation. The aforementioned synergistic effects collectively endow the IMCA-10 film with exceptional EMI shielding performance.

3.4. Joule heating performance and antibacterial property of the films

The IMCA-10 film can also serve as a Joule heater (Fig. 5a), showcasing huge potential in wearable electronics. As depicted in Fig. 5b, the surface temperature of the IMCA-10 film quickly reaches approximately 40 ℃ upon a relatively low voltage of 1.0 V. This temperature responds quickly to the input voltage, rising significantly with increasing voltage until reaching a steady-state saturation value. For example, when subjected to an input voltage of 2.5 V, the temperature rises to 126 ℃ rapidly, and upon removal of the voltage, it falls back to room temperature quickly. As shown in Fig. 5c, the equilibrium temperature of the IMCA-10 film presents a strong linear relationship with the square of the applied voltage (U^2) in accordance with Joule's law [52], suggesting tunable thermal management. Fig. 5d exhibits the infrared thermal images of the film at saturation temperatures under various driving voltages. Fig. 5e illustrates the temperature evolution of the IMCA-10 film under stepwise voltage. When the applied voltage is increased or decreased, the film shows a rapid and delay-free temperature response. Fig. 5f demonstrates the excellent cyclic heating stability. Furthermore, the IMCA-10 film is capable of maintaining a stable temperature of 126 ℃ under a voltage of 2.5 V for up to 1200 s, which indicates the excellent reliability and durability (Fig. 5g). The infrared images (Fig. 5g, inset)

Just Accepted

reveal the uniform and steady surface temperature. As shown in Fig. 5h, at a low voltage of 2.0 V, the ice on the film surface melts within 40 s, offering an effective de-icing approach for cold-region electric equipment. Therefore, due to these excellent features of adjustable temperature, low driving voltage, and remarkable stability and durability, the IMCA-10 film holds considerable potential for applications in wearable warming technology and intelligent heating devices.

We also demonstrate the antibacterial properties of the IMCA films that are essential for wearable electronic applications. The plate colony counting method is employed to visually showcase the inhibitory effect of the IMCA-10 film against Gram-negative E. coli and Gram-positive S. aureus. As shown in Figs. 5i and j, the control groups display a large number of bacterial colonies but the experimental groups exhibit an impressive antibacterial efficiency, approaching 99.99%. These results suggest that the IMCA-10 film possesses excellent antibacterial properties, which is ascribed to the release of free Ag^+ ions that can penetrate bacterial cells and readily bind to the sulfhydryl (-SH) groups of proteases [53], thereby inactivating these enzymes.

3.5. Self-powered sensing and information transmission applications of the IMCA film

We explore the mechanically robust and highly conductive IMCA films as self-powered sensor for human motion detection, information coding and transmission for wearable electronics. The IMCA-10 film is employed as an electrode in a single-electrode mode triboelectric nanogenerator (TENG). Fig. S19a shows the structure and working mechanism of the TENG under the contact-separation mode. When IMCA-10 film and PDMS layer are in full contact with each other under a compressive force, the triboelectric effect can generate equal but opposite friction charges on their surfaces. As the external force is released and the two layers separate, free electrons are propelled from the ground towards the IMCA-10 film due to the electrostatic field effect, thereby inducing a transient current [54]. When they are completely separated, the positive charges on the IMCA-10 film are fully neutralized and the system attains electrostatic equilibrium, causing no free electron movement in the circuit. The subsequent re-approach of the PDMS layer towards the IMCA-10 film triggers the reverse process, in which transient electrons flow from the IMCA-10 film to the ground via the external circuit, thus generating a reverse current. When the IMCA-10 film makes full contact with the PDMS layer again, the system returns to its initial state. Through

Just Accepted

repeated contact-separation cycles between the PDMS and IMCA-10 film, the film-based TENG is capable of generating periodic electrical output signals.

We investigate the output performance metrics, such as open-circuit voltage (Voc), short-circuit current (Isc) and transferred charge (Qsc) of the as-fabricated TENG under varying pressures and frequencies. The IMCA-10 film-based TENG achieves a maximum Voc (111 V) under an internal force of 20 N and a frequency of 2 Hz (Fig. S19b). Notably, the increasing pressure from 5 N to 20 N can remarkably boost the output performance of the TENG (Figs. S19b-d). The Voc, Isc and Qsc increase from 51 V, 0.14 μA and 11.6 nC to 111 V, 0.35 μA and 30 nC. This enhancement can be ascribed to the poles moving closer together as the external pressure increases, thereby accelerating electron transfer [55]. As the frequency increases from 1 Hz to 4 Hz, the Voc and Qsc exhibit negligible changes, stabilizing at 111 V and 30 nC (Figs. S19e and g). However, the Isc rises from 0.24 μA to 0.42 μA (Fig. S19f), resulting from increased frequency enhancing charge accumulation speed [56].

Furthermore, the IMCA-10 film-based TENG serves as a self-powered human motion sensor in a continuous, real-time and non-invasive mode due to its excellent mechanical properties and efficient output performance. As shown in Fig. 6a, most human joint movements primarily involve bending actions, particularly those of the throat, elbow, wrist, finger, knee and ankle. The PDMS-encapsulated IMCA-10 film-based TENG (Fig. S20) with a length of 20 mm and width of 15 mm can be attached to different parts of the human skin. Upon joint flexion, the film undergoes compressive deformation, generating induced charges in the electrode. Subsequent extension releases the deformation, driving a reverse current through the external circuit. The film-based sensor generates distinct Voc signals in response to varying bending amplitudes. Compared with the small-amplitude throat vibration, wrist and finger bending (Figs. 6b-d, f), the IMCA-10 film exhibits a significantly higher Voc for larger limb movements (elbow and knee bending) (Figs. 6e and g), indicating enhanced signal output with larger bending amplitudes. The sensor exhibits remarkable sensitivity in detecting both large-scale movements and subtle motions. We also demonstrate the long-term stability of the IMCA-10 film-based TENG by measuring the output voltage over 4000 cycles of contact-separation, which remains almost constant, indicating stable operational performance as wearable electronics during long-term use (Fig. 6h).

To further validate its wide range of applications, we conduct self-powered information

Just Accepted

coding and transmission tests for the IMCA film. Based on the triboelectric effect, upon pressing the TENG with a finger, electrons are transferred from the skin to the surface of PDMS because PDMS exhibits a higher electron affinity than skin, thereby leaving the skin positively charged and the PDMS negatively charged (Fig. 7a). Alternating contact and separation between the finger and the TENG then generate an output voltage signal. International Morse Code, a standardized coding system consisting of dots and dashes, can be represented by intermittent pressing, continuous pressing, and pauses inserted between each letter [57]. Based on the finger's contact and separation from the TENG, the voltage signals are defined by skin contact duration: prolonged tapping as the dash "-" and brief tapping as the dot "·" (Fig. 7b). Accordingly, the message of "HELLO" can be effectively expressed and transmitted in specific sequences of "-" and "·" by rhythmically pressing the sensor (Fig. 7c). Following the same protocol, other critical messages such as "SOS", "HELP" and "SUSTech" can also be similarly represented by their generated corresponding voltage signals (Figs. 7d-f). When individuals are in danger and unable to call for help directly, this information transmission method can relay their location and status to ensure timely access to assistance.

We further explore the film-based self-powered sensor for handwriting and machine learning-assisted recognition. Fig. 7g illustrates the mechanism of the handwriting sensing by converting them to specific electrical signals corresponding to different symbols written on its surface. Each symbol yields a unique voltage signal with a highly consistent and reproducible waveform (Figs. 7h-l). Following the acquisition of voltage signals corresponding to five distinct symbols, we employ a convolutional neural network (CNN) integrated with a self-attention mechanism to achieve efficient and accurate handwritten symbol recognition (Fig. 7m). A dataset comprising 100 trials per symbol is randomly partitioned into training (80%) and testing (20%) subsets. After 50 training epochs, the model achieves stability, as indicated by the training accuracy and loss curves (Fig. 7n). The confusion matrix further confirms high-fidelity prediction across all symbols, yielding an average recognition accuracy of 100% (Fig. 7o). By mapping specific symbols to distinct health statuses of the wearer, the wearer can promptly convey their condition by writing the corresponding symbols, which are subsequently transmitted wirelessly to a physician for emergency assistance and diagnostic purposes. Collectively, these results underscore the practical and diverse applications of our self-powered sensing platform in the fields

Just Accepted

of motion monitoring and intelligent data transmission.

4. Conclusions

In summary, we have demonstrated a multiscale-reinforced high-strength IMCA composite film with integrated multifunctionality for next-generation electromagnetic protection and intelligent sensing applications. By synergistically combining sandwich and nacre-like architectures with molecular-level crosslinking, the IMCA film breaks the trade-off between EMI shielding performance and mechanical properties of conventional EMI shielding films and achieves a tensile strength of up to 315 MPa and an exceptional EMI SE of 62 dB and SSE/t of 16550 $dB \cdot cm^2 \cdot g^{-1}$. Furthermore, the film shows remarkably efficient low-voltage-driven Joule heating performance, excellent antibacterial properties and outstanding self-powered sensing capabilities encompassing human motion monitoring, information coding and transmission. By incorporating a machine learning algorithm, a perfect accuracy in handwriting recognition can be achieved. This research not only provides an innovative and practical strategy for the design and preparation of multifunctional EMI shielding composite films with exceptional mechanical properties, but also broadens their potential applications for advanced wearable electronics.

Acknowledgements

This work was supported by the National Natural Science Foundation of China (12588301, 12272159), the Guangdong S&T Programme (2024B1212010003, 2023ZT10Z002), and the Shenzhen Science and Technology Innovation Bureau (2025562891, KQTD20240729102052065). L. Yu would like to acknowledge the technical support from SUSTech CRF.

References

[1] Liu, A.; Zhang, Y. L.; Xu, X. S.; Kong, J.; Gu, J. W. Multi-field synergy for orchestrating filler angles in polyimide aerogels with switchable electromagnetic interference shielding. *Adv. Mater.* **2026**, 38, e73267.

[2] Ma, G. S.; Li, J.; Yan, Y. F.; Qin, G. Y.; Gao, B. S.; Chen, T.; Cheng, Z. Y.; Huang, X. X. Carbon-transition metal dichalcogenide composites: A comprehensive review on electromagnetic wave absorption. *Carbon* **2025**, 244 120690.

[3] Hu, X. F.; Zhai, M. Z.; Zhang, Y. L.; Wang, L.; Gu, J. W. Multiple hydrogen-bonding network engineered multi-layered polyurethane aerogels for absorption-dominant electromagnetic interference shielding. *Adv. Funct. Mater.* **2026**, 36, e78248.

Just Accepted

[4] Yan, Y. F.; Qin, G. Y.; Zhang, K. L.; Gao, B. S.; Ma, G. S.; Huang, X. X.; Zhou, Y. Enhancing microwave absorption performance of MoS_2 by synergistic effect of Fe doping. *J. Adv. Ceram.* **2025**, 14, 9221039.

[5] Hu, X. F.; Zhang, Y. L.; Guo, H.; He, M. K.; Qiu, H.; Shi, X. T.; Wang, L.; Gu, J. W. Multifunctional flexible WPU composite aerogels with sandwich structure for dual-sided low-reflection electromagnetic interference shielding. *Adv. Funct. Mater.* **2026**, 36, e17665.

[6] Gao, B. S.; Yan, Y. F.; Zhang, K. L.; Liu, D. D.; Huang, X. X. Ultralight broadband electromagnetic wave absorption enabled by interface-engineered two-layered periodic carbon fiber fabrics. *Adv. Funct. Mater.* **2026**, 36, e32108.

[7] Qin, G. Y.; Liu, Y. N.; Yan, Y. F.; Ma, G. S.; Gao, B. S.; Cheng, Z. Y.; Chen, T.; Huang, X. X. Continuously adjustable impedance gradient in laminar aerogels: Synergizing matching and multi-position attenuation for broadband absorption. *Adv. Funct. Mater.* **2026**, 36, e19796.

[8] Yan, Y. F.; Cheng, Z. Y.; Chen, T.; Zhou, E.; Gao, B. S.; Qin, G. Y.; Ma, G. S.; Huang, X. X. Rational high-entropy doping strategy via modular in situ/post solvothermal doping integration for microwave absorption. *J. Adv. Ceram.* **2025**, 14, 9221168.

[9] Yu, L. F.; Luo, S.; Yang, Y. N.; Huang, X. Y.; Xiao, Y. H.; Chen, Q.; Fu, L. S.; Liu, R. P.; Xia, L.; Xue, Y. H. Robust multifunctional MXene-based composite films with Janus-like structure for high-performance electromagnetic interference shielding, electrothermal conversion and infrared stealth. *J. Alloys Compd.* **2026**, 1051, 186036.

[10] Li, S.; Zhou, J. Y.; Miao, M.; Qian, K. P.; Fang, J. H.; Feng, X. $Ti_3C_2T_x$ MXene-mediated sensitization-metallization enables sandwich-structured copper@aramid films for high-performance electromagnetic interference shielding. *Nano Res.* **2026**, 19, 94908304.

[11] Yu, L. F.; Yang, Y. N.; Huang, X. Y.; Xiao, Y. H.; Fu, L. S.; Liu, R. P.; Xia, L.; Xue, Y. H. Multiscale-reinforced high-strength MXene-based EMI shielding films with integrated electronic skin functionalities. *Chem. Eng. J.* **2026**, 530, 173663.

[12] Jia, S. S.; Guo, C. Q.; Shi, X. Y.; Jiao, J. P.; Zhang, Y.; Lu, Y. X.; Wang, G. B.; Zhang, S. L. All-in-one Janus-type membrane with asymmetric gradient for dual-mode thermal management, EMI shielding and motion perception. *Chem. Eng. J.* **2026**, 542, 178000.

[13] Liu, Z.; Xue, Y. H.; Meng, Y. T.; Wang, J. E.; Zhang, H.; Zhang, F. J.; Meng, F. B.; Zhao, B.; Yan, L. T.; Liang, B. L. Reduced-reflectance bionic E-skin with

Just Accepted

electromagnetic-environmental-sensing integration enabled by Ni-reconstructed liquid metal networks. *Adv. Funct. Mater.* **2026**, 36, e76178.

[14] Zhai, M. Z.; Zhao, S. J.; Guo, H.; Li, X. C.; Shi, X. T.; He, M. K.; Zhang, Y. L.; Gu, J. W. Bionic-structured electromagnetic interference shielding composites. *Sci. Bull.* **2025**, 70, 2347-2364.

[15] Yu, L. F.; Huang, X. Y.; Xiao, Y. H.; Chen, Q.; Luo, S.; Fu, L. S.; Liu, R. P.; Xue, Y. H. Robust cellulose-carbon nanotube composite film with sandwiched silver nanowires for ultra-efficient electromagnetic interference shielding and Joule heating. *J. Alloys Compd.* **2025**, 1041, 183888.

[16] Zhao, Y. M.; Sun, S.; Yang, L. S.; Yang, Y. H.; Wang, Z. Y.; Ye, Z. M.; He, S. L.; Zhang, Y.; Liu, B. L.; Cao, A. Y.; et al. Polymer-assisted co-exfoliation-assembly of pristine graphene-based films for integrated terahertz shielding and thermal management. *Adv. Funct. Mater.* **2025**, 36, 2522073.

[17] Yu, L. F.; Yang, Y. N.; Chang, S. L.; Xiao, Y. H.; Luo, S.; Hao, S. C.; Fu, L. S.; Liu, R. P.; Xia, L.; Xue, Y. H. Interdigitated electric-magnetic gradient MXene-based nanocomposite films for concurrent high-efficiency electromagnetic shielding and sensitive detection. *Chem. Eng. J.* **2026**, 543, 178533.

[18] Zhang, Y. L.; Ruan, K. P.; Zhou, K.; Gu, J. W. Controlled distributed $Ti_3C_2T_x$ hollow microspheres on thermally conductive polyimide composite films for excellent electromagnetic interference shielding. *Adv. Mater.* **2023**, 35, 2211642.

[19] Li, T.; Yang, Y. J.; Fan, Y. W.; Huang, D. Y.; Zhang, L.; Hu, X. P.; Chen, Y.; Sheng, X. X. Layered MXene-phase change composites for integrated photothermal regulation and electromagnetic shielding. *Nano Res.* **2026**, 19, 94908054.

[20] Si, Z. K.; Yan, Y. Z.; Liu, X.; Xu, L. L.; Liao, H. X.; Nie, Z.; Xue, C. H.; Wan, G. P.; Wang, G. Z. Flexible and multifunctional microcrystalline cellulose/$Ti_3C_2T_x$ MXene-POSS composite films for electromagnetic interference shielding in extreme environments. *Chem. Eng. J.* **2025**, 525, 169897.

[21] Yang, Z. L.; Ren, W. N.; Lang, L.; Wang, R. M.; Hu, J. R.; Wang, L. Multifunctional EMI shielding aramid nanofibers films with record-breaking electrical conductivity enabled by solid-liquid bicontinuous conductive network. *Adv. Funct. Mater.* **2026**, 36, e74892.

Just Accepted

[22] Zhang, H.; Wang, J. E.; Zhang, Y. L.; Meng, Y. T.; Xue, Y. H.; Liu, Z.; Liang, B. L.; Gu, J. W. MoS_2 nanoflower-mediated MXene/ANF composite films with simultaneous strength-toughness synergy and high-efficient electromagnetic interference shielding. *Adv. Funct. Mater.* **2026**, 36, e78516.

[23] Wang, Y. H.; Pang, K. X.; Zhao, L. L.; Zhang, J. W.; Zhang, Y.; Zhao, Y. X.; Gong, C. H.; Zhou, S. S.; Zhang, J. W. Directional dispersion of ultralong single-walled carbon nanotubes induced by solvent crystallization for effective electromagnetic interference shielding. *Nano Res.* **2026**, 19, 94908280.

[24] Liu, Y.; Wu, N.; Pan, F.; Zheng, S. N.; Liu, W.; Liu, J. R.; Zeng, Z. H. Energy-efficiency-dried silver nanowire aerogels with orientational-tunable gigahertz and terahertz electromagnetic-interference shielding. *Adv. Funct. Mater.* **2026**, 36, e29559.

[25] Hang, T. Y.; Zhou, L. J.; Xu, C. H.; Chen, Y. M.; Shen, J. H.; Zheng, J. J.; Yang, P. A.; Li, X. P.; Luo, H.; Tong, G. X. High-performance wearable bimetallic nanowire-assisted composite foams for efficient electromagnetic interference shielding, infrared stealth, and piezoresistive sensing. *Nano Res.* **2024**, 17, 6757-6765.

[26] Wei, J. Y.; Cai, X. X.; Hu, J. W.; Lin, S. D. Multifunctional AgNWs-Fe_3O_4/ANF composite films with a Janus-like structure for outstanding electromagnetic interference shielding and thermal management. *J. Mater. Chem. A* **2025**, 13, 5789.

[27] Wang, J. Y.; Zhang, Q.; Zhang, S.; Liu, R. Z.; Zhang, Y.; Wang, Y. M.; Ming, J. F. Multifunctional polysulfonamide/AgNWs aerogel for electromagnetic interference shielding. *Compos. Commun.* **2025**, 56, 102346.

[28] Li, L.; Yan, Y. Z.; Liang, J. F.; Zhao, J. C.; Lyu, C. Y.; Zhai, H. X.; Wu, X. L.; Wang, G. Z. Wearable EMI shielding composite films with integrated optimization of electrical safety, biosafety and thermal safety. *Adv. Sci.* **2024**, 11, 2400887.

[29] Chen, Y. M.; Pang, L.; Li, Y.; Luo, H.; Duan, G. G.; Mei, C. T.; Xu, W. H.; Zhou, W.; Liu, K. M.; Jiang, S. H. Ultra-thin and highly flexible cellulose nanofiber/silver nanowire conductive paper for effective electromagnetic interference shielding. *Compos. A: Appl. Sci. Manuf.* **2020**, 135, 105960.

Just Accepted

[30] Teng, R.; Sun, J. M.; Nie, Y. X.; Li, A. Q.; Liu, X.; Sun, W. Y.; An, B.; Ma, C. H.; Liu, S. X.; Li, W. An ultra-thin and highly efficient electromagnetic interference shielding composite paper with hydrophobic and antibacterial properties. *Int. J. Biol. Macromol.* **2023**, 253, 127510.

[31] Dai, Y. H.; Sun, N.; Jiang, D. X.; Wang, Z. F.; Ding, Q.; Zhang, Z.; Liu, Y. Ultrathin and highly flexible layered silver nanowires/carboxymethyl cellulose nanofiber nanocomposite films for electromagnetic interference shielding. *Int. J. Biol. Macromol.* **2024**, 278, 134770.

[32] Li, S.; Qian, K. P.; Thaiboonrod, S.; Wu, H. M.; Cao, S. M.; Miao, M.; Shi, L. Y.; Feng, X. Flexible multilayered aramid nanofiber/silver nanowire films with outstanding thermal durability for electromagnetic interference shielding. *Compos. A: Appl. Sci. Manuf.* **2021**, 151, 106643.

[33] Wan, S. J.; Li, Xi.; Chen, Y.; Liu, N. N.; Du, Y.; Dou, S. X.; Jiang, L.; Cheng, Q. F. High-strength scalable MXene films through bridging-induced densification. *Science* **2021**, 374, 96-99.

[34] Wang, S. W.; Ma, Y. Y.; Zhu, S. L.; Ma, H. Y.; Yue, Y. Y.; Wu, Q. L.; Xiao, H. N.; Han, J. Q. Biomimetic and electrostatic self-assembled nanocellulose/MXene films constructed with sequential bridging strategy for flexible supercapacitor. *Chem. Eng. J.* **2024**, 495, 153552.

[35] Lew, A. J.; Stifler, C. A.; Tits, A.; Schmidt, C. A.; Scholl, A.; Cantamessa, A.; Müller, L.; Delaunois, Y.; Compère, P.; Ruffoni, D.; et al. A molecular-scale understanding of misorientation toughening in corals and seashells. *Adv. Mater.* **2023**, 35, 2300373.

[36] Wei, J.; Ma, C.; Zhang, T. T.; Shao, Z. Q.; Chen, Y. X. High-performance cellulose nanofibers-based actuators with multi-stimulus responses and energy storage. *Chem. Eng. J.* **2024**, 490, 151393.

[37] Han, M. M.; Shen, W. H. Nacre-inspired cellulose nanofiber/MXene flexible composite film with mechanical robustness for humidity sensing. *Carbohydr. Polym.* **2022**, 298, 120109.

[38] Han, M. M.; Shen, W. H.; Corriou, J. P. Polydopamine-modified MXene/cellulose nanofibers composite film for self-powered humidity sensing and humidity actuating. *Nano Energy* **2024**, 123, 109445.

[39] Fei, W. K.; Wang, X. J.; Miao, C. Y.; Chen, J. H.; Liu, S. J.; Li, B. X.; Li, J. M.; Zhao, Q. Fe^{2+}-crosslinked MXene fibers for multifunctional electronic textile. *Nano Res.* **2026**, 19, 94908426.

Just Accepted

[40] Zhu, L. Y.; Yang, H. B.; Xu, T.; Wang, L. Y.; Lei, J. D.; Si, C. L. Engineered nanochannels in MXene heterogeneous proton exchange membranes mediated by cellulose nanofiber/sodium alginate dual crosslinked networks. *Adv. Funct. Mater.* **2024**, 24, 2419334.

[41] Wu, K.; Liu, Y. D.; Geng, C. Z.; Li, X. K. Ultra-compact MXene/alginate/PVA composite fibers by intercalation and chelation for enhanced flame retardancy and energy harvesting. *Small* **2025**, 21, 2411459.

[42] Cao, X. H.; Wu, G. Q.; Li, K. R.; Hou, C. Y.; Li, Y. G.; Zhang, Q. H.; Wang, H. Z. High-performance Zn^{2+}-crosslinked MXene fibers for versatile flexible electronics. *Adv. Funct. Mater.* **2024**, 34, 2407975.

[43] Hao, Y.; Zhang, Z. X.; Chen, Y. J.; Wang, S.; Tong, Y. J.; Lv, P. F.; Wei, Q. F.; Lee, C. K. Strong and tough MXene‐induced bacterial cellulose macrofibers for AIoT textile electronics. *Nano-Micro Lett.* **2026**, 18, 198.

[44] Wang, H. Y.; Li, Y. Z.; Liu, J. H.; Wan, X. F.; Li, Y. C.; Xu, G. C.; Yuan, H. C.; Wang, S. Y.; Xu, P.; Xu, M. Y. A flexible wearable single-electrode triboelectric sensor based on self-healing ionic elastomer for reliable underwater motion sensing. *Chem. Eng. J.* **2026**, 537, 176192.

[45] Wang, Y. Q.; Chen, P. C.; Ding, Y.; Zhu, P. H.; Liu, Y. T.; Wang, C. X.; Gao, C. H. Multifunctional nano‐conductive hydrogels with high mechanical strength, toughness and fatigue resistance as self-powered wearable sensors and deep learning-assisted recognition system. *Adv. Funct. Mater.* **2024**, 34, 2409081.

[46] Wang, W. Y.; Guo, P. S.; Liu, X.; Chen, M. J.; Li, J. H.; Hu, Z. G.; Li, G. D.; Chang, Q.; Shi, K. M.; Wang, X. L.; et al. Fully polymeric conductive hydrogels with low hysteresis and high toughness as multi-responsive and self-powered wearable sensors. *Adv. Funct. Mater.* **2024**, 34, 2316346.

[47] Zong, X. J.; Liu, Q. K.; Zhang, N. Q.; Wang, J. L.; Zhang, C. P. Skin-inspired self-assembled gradient hetero-interlocked nanofibers tactile sensor for handwritten gesture recognition. *Chem. Eng. J.* **2026**, 530, 173575.

[48] Lin, L. Q.; Wang, W. T.; Huang, J. L.; Li, Q. B.; Sun, D. H.; Yang, X.; Wang, H. X.; He, N.; Wang, Y. P. Nature factory of silver nanowires: Plant-mediated synthesis using broth of Cassia fistula leaf. *Chem. Eng. J.* **2010**, 162, 852-858.

Just Accepted

[49] Yu, J. W.; Gu, W. H.; Zhao, H. Q.; Ji, G. B. Lightweight, flexible and freestanding PVA/PEDOT: PSS/AgNWs film for high-performance electromagnetic interference shielding. *Sci. China Mater.* **2021**, 64, 1723-1732.

[50] Jia, Y. Y.; Fu, J. S.; Zhang, Z. J.; Yan, J.; Zhang, Y. F.; Cheng, Q. F. Strong MXene induced conductive silk fibers. *Adv. Mater.* **2025**, 37, 2501420.

[51] Wang, B. Z.; Huang, P.; Li, B. J.; Wu, Z.; Xing, Y. Q.; Liu, L. Construction of MXene interlayer conductive ion transport channel by polypyrrole-coated cellulose nanofibers for ultra-low voltage high-performance ionic soft actuators. *Sens. Actuators B: Chem.* **2025**, 422, 136649.

[52] Chen, T.; Yan, Y. F.; Liu, S. Q.; Cheng, Z. Y.; Gao, B. S.; Jia, D. C.; Zhou, Y.; Huang, X. X. Lightweight and flexible fabric assembled by ANF/GMWCNT fibers for broadband electromagnetic wave absorption. *Adv. Funct. Mater.* **2026**, 36, e28094.

[53] Zha, J. J.; Sun, T.; Kong, L.; Liu, C. Q.; Sun, H. M.; Wang, D.; Ni, G. H. Plasma synthesis of amine-fluorocarbon polymer functionalized mesoporous silica-supported silver nanoparticles for enhanced antibacterial efficacy. *Chem. Eng. J.* **2025**, 522, 167038.

[54] Yu, G.; Hu, H.; Yu, Q. G.; Li, C.; Zhou, D. D.; Wang, Z. K.; Bi, K. D. Fiber composites-based flexible triboelectric nanogenerators: From material design to emerging applications. *Int. J. Extreme Manuf.* **2026**, 8, 012010.

[55] Li, Z. K.; Liu, J. T.; Chi, M. S.; Miao, X.; Yang, H. X.; Cui, W. Q.; Yu, A. F.; Zhai, J. Y. Ultra-high output triboelectric nanogenerator based on synergies of material modification and charge pumping. *Chem. Eng. J.* **2024**, 481, 148726.

[56] Wu, G. L.; Pan, J. J.; Xia, W.; Xiao, P.; Fan, H. H.; Liu, B. C.; Lavorgna, M.; Liu, J. Z.; Cai, G. M. Cross-scale regulation of coaxial twisted core-sheath composite yarn for constructing permeable intelligent fabric with multiple protection and perception. *Adv. Funct. Mater.* **2025**, 35, 2503613.

[57] Ma, J. R.; Li, S. N.; Gu, Y. J.; Wang, D. N.; Yang, W. S.; Mei, C. T.; Xu, X. W.; Xiao, H. N.; Han, J. Q. Innovative cellulose-mediated liquid metal composites hydrogel with adhesive and mechanical-thermal multimodal sensing capabilities for smart wearable devices. *Chem. Eng. J.* **2026**, 530, 173583.

Just Accepted

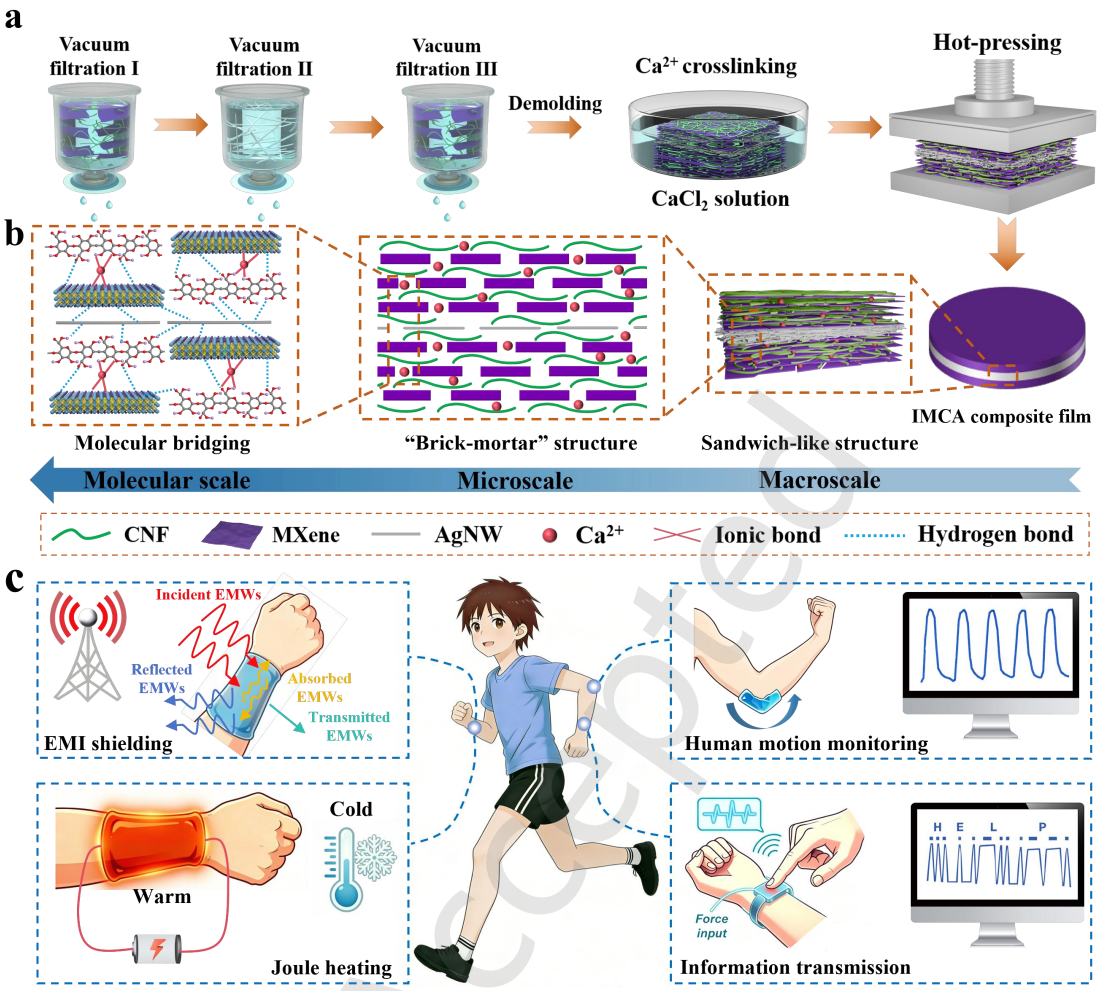


Figure 1 Schematic diagram of the preparation, hierarchical structure and multifunctionality of the IMCA composite films. (a) The fabrication of the IMCA film. (b) Hierarchical structure of the IMCA film. (c) Potential applications of the multifunctional IMCA film: EMI shielding, Joule heating, human motion monitoring and information transmission.

Just Accepted

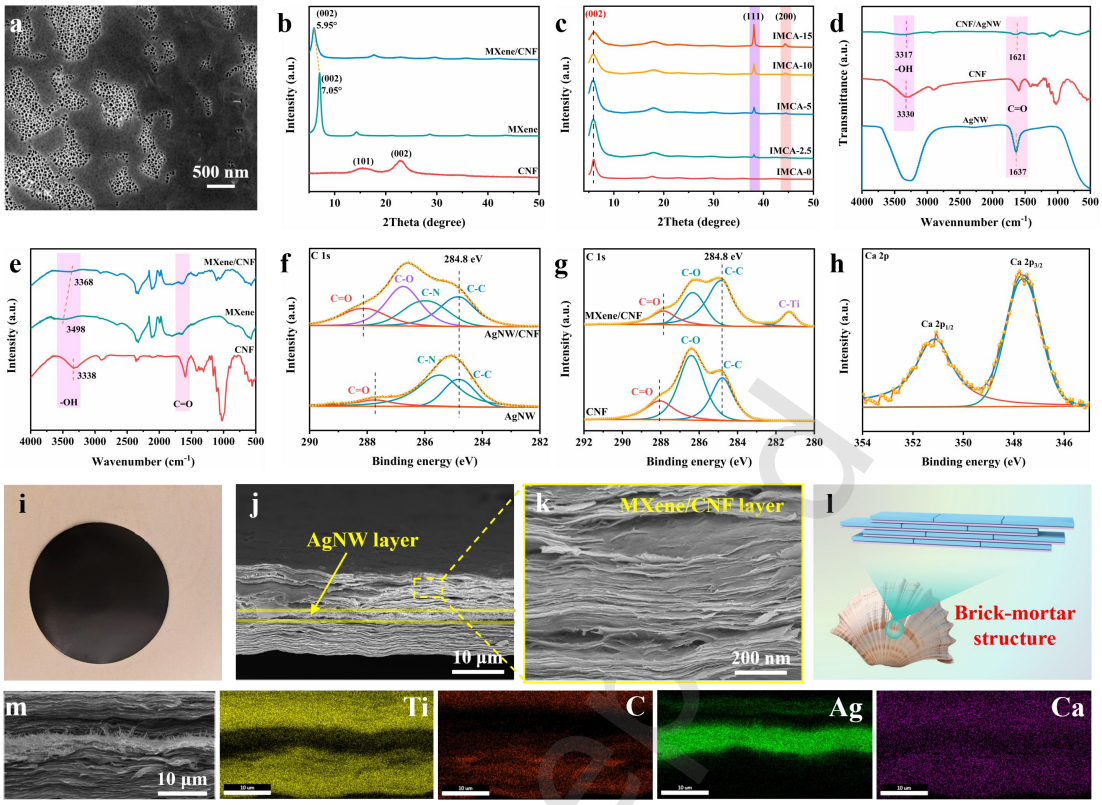


Figure 2 Structural, component and morphology characterization. (a) SEM image of the MXene. (b) XRD patterns of the CNF, MXene and MXene/CNF. (c) XRD patterns of the IMCA-X films. (d) FTIR spectra of the AgNW, CNF and CNF/AgNW. (e) FTIR spectra of the CNF, MXene and MXene/CNF. (f) High-resolution C 1s spectra of the AgNW and AgNW/CNF. (g) High-resolution C 1s spectra of the CNF and MXene/CNF. (h) High-resolution Ca 2p spectrum of the IMCA-10 film. (i) Digital image of the IMCA-10 film. (j and k) Cross-sectional SEM images of the IMCA-10 film. (l) Schematic of the natural nacre. (m) Cross-sectional EDS mapping images of the IMCA-10 film.

Just Accepted

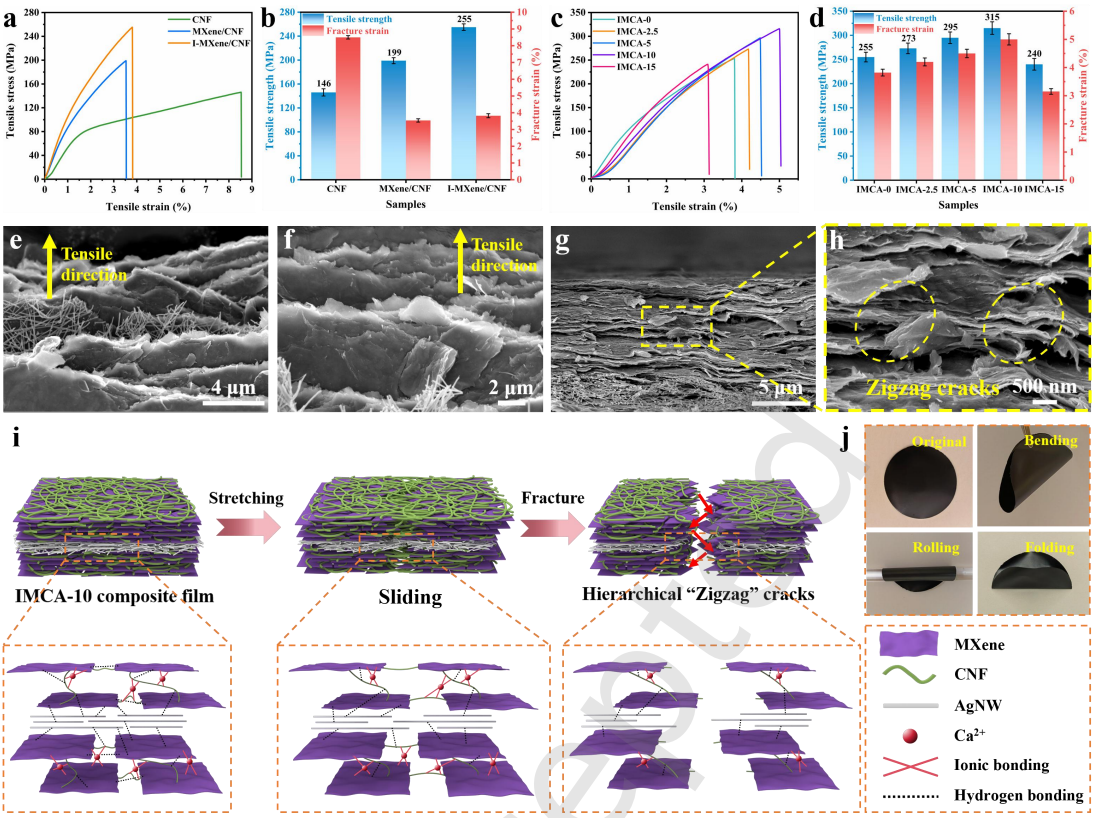


Figure 3 Mechanical properties of the IMCA films. (a) Tensile stress-strain curves and (b) the corresponding tensile strength and fracture strain of the CNF, MXene/CNF and I-MXene/CNF films. (c) Tensile stress-strain curves and (d) the corresponding tensile strength and fracture strain of the IMCA-X films. SEM images of the fracture surface (e and f) and cross section (g and h) after stretching of the IMCA-10 film. (i) Fracture mechanism of the IMCA-10 film. (j) Flexibility demonstration of the IMCA-10 film.

Just Accepted

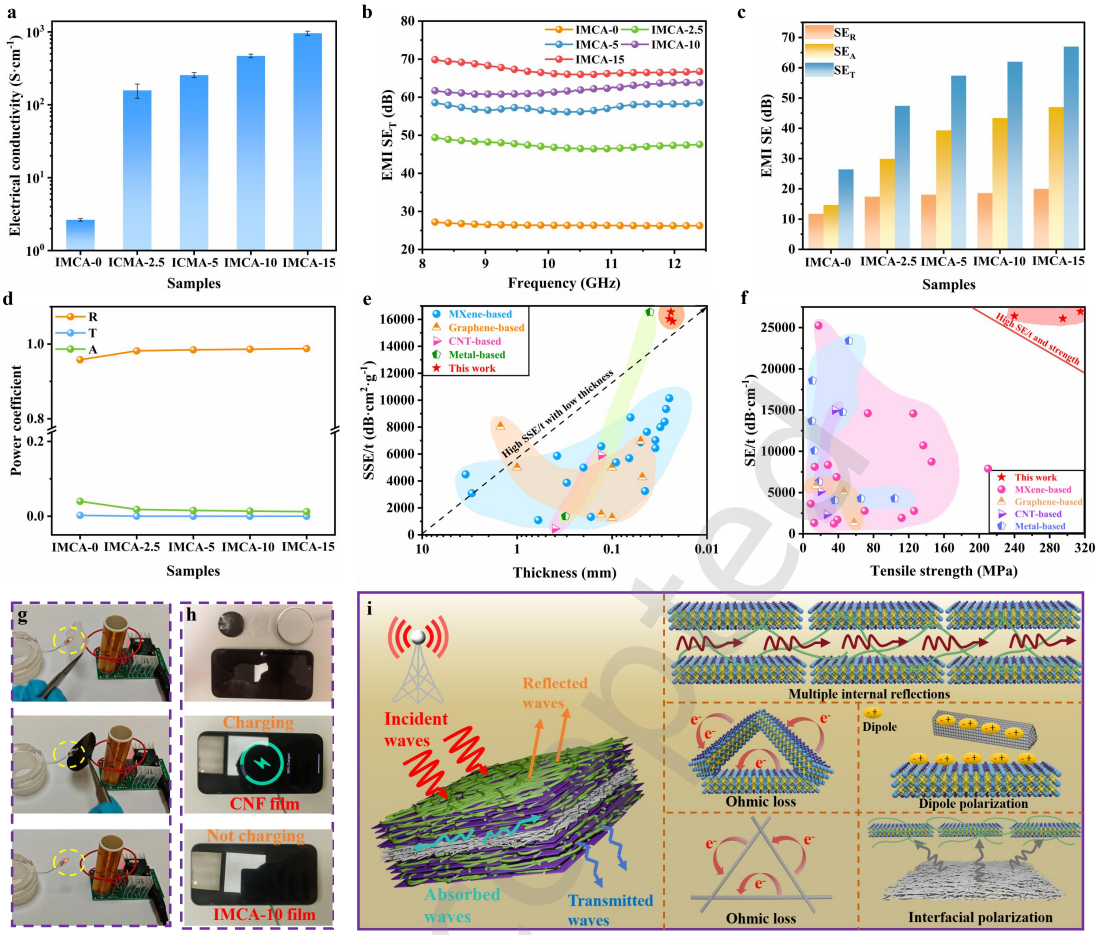


Figure 4 EMI shielding performance and practical application of the IMCA-X films. Electrical conductivity (a) and EMI SE (b) of the IMCA-X films. (c and d) EMI shielding efficiency (SE_R, SE_A and SE_T) and power coefficient (A, R and T) of the IMCA-X films. (e) Comparison of thickness and EMI SSE/t with those of other reported materials. (f) Comparison of tensile strength and EMI SE/t with those of other reported materials. (g and h) Demonstrations of the practical application of the IMCA-10 film. (i) EMI shielding mechanism of the IMCA-10 film.

Just Accepted

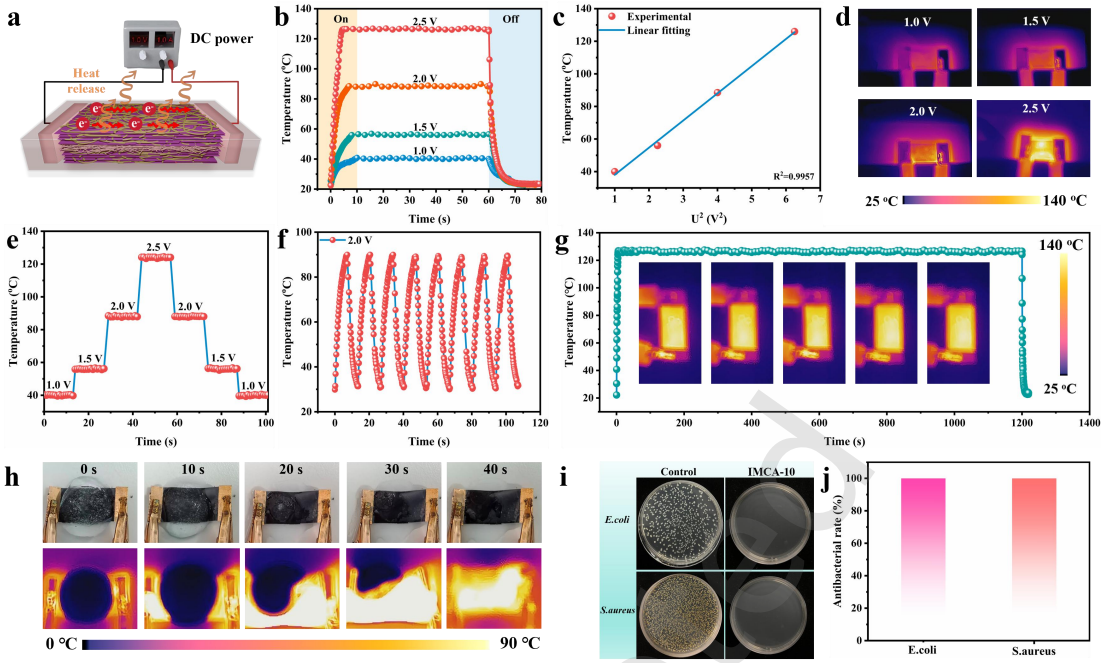


Figure 5 Joule heating performance and antibacterial property of the IMCA-10 film. (a) Schematic illustration of Joule heating. (b) Temperature-time variation curves of the IMCA-10 film at different voltages. (c) Relationship between saturation temperature and U^2. (d) IR images of saturation temperature upon varying voltages. (e) Real-time temperature response at continuously changing voltages. (f) Temperature response under repeated on/off cycling under a voltage of 2.0 V. (g) Long-term Joule heating curve under a voltage of 2.5 V. (h) Ice-melting test with a voltage of 2.0 V. (i) Digital photos of the colonies. (j) The antibacterial rates of the IMCA-10 film against E. coli and S. aureus after 24 h of co-cultivation.

Just Accepted

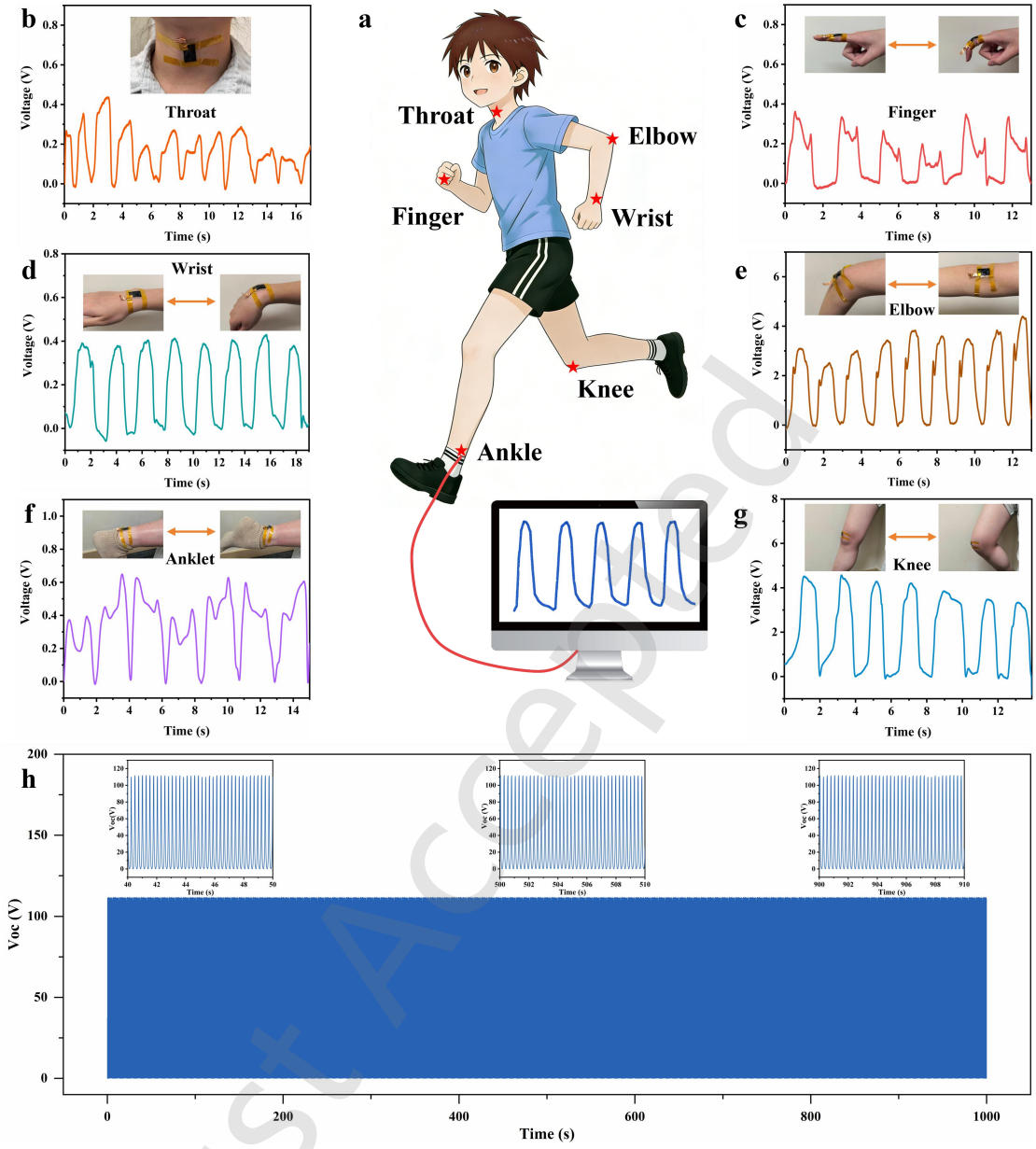


Figure 6 Wearable IMCA-10 film for self-powered human activity monitoring. (a) Schematic illustration of the sporting monitoring. Voltage response curves for different parts of human body: (b) throat, (c) finger, (d) wrist, (e) elbow, (f) ankle and (g) knee. (h) Stability of the IMCA-10 film-based TENG at 4 Hz and 20 N for 4000 contact separation cycles.

Just Accepted

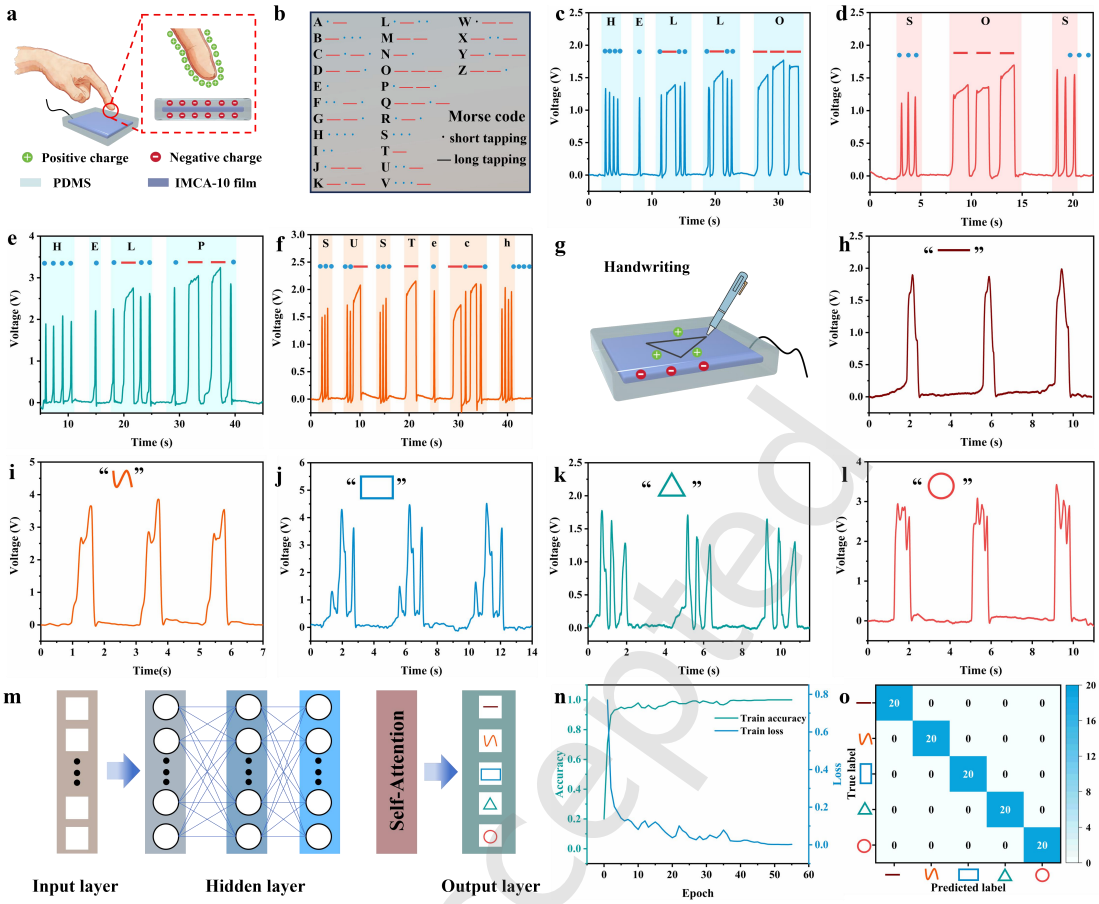


Figure 7 The film-based self-powered sensor applied to information transmission. (a) Working principle of the IMCA-10 film-based self-powered sensor for Morse code compilation. (b) Schematic illustration of the international Morse code. The voltage output signal corresponding to Morse code of various characters: (c) “HELLO”, (d) “SOS”, (e) “HELP” and (f) “SUSTech”. (g) Working principle of the IMCA-10 film-based self-powered sensor for handwriting. The voltage output signal corresponding to various symbols: (h) “Straight line”, (i) “Curve”, (j) “Rectangle”, (k) “Triangle” and (l) “Circle”. (m) Schematic illustration of the machine learning algorithm. (n) Training accuracy and loss function under different epochs. (o) Confusion matrix of symbol identification results.

Just Accepted

Electronic Supplementary Material

Ultrathin and efficient wearable EMI shields with integrated self-powered sensing and information coding

Lingfeng Yu[1,2], Yanni Yang[3], Yihao Xiao[1,2], Song Luo[1], Shichun Hao[3], Jingzhe Yang[3], Qiang Chen [1], Lishun Fu[2*], Long Xia[3], Yahui Xue[1,4*]

[1] Department of Mechanics and Aerospace Engineering, and Center for Complex Flows and Soft Matter Research, Southern University of Science and Technology, Shenzhen 518055, China

[2] Shenzhen Key Laboratory of Transformation Optics and Spatial Modulation, Kuang-Chi Institute of Advanced Technology, Shenzhen 518057, China

[3] School of Materials Science and Engineering, Harbin Institute of Technology (Weihai), Weihai 264209, China

[4] Guangdong Provincial Key Laboratory of Sustainable Biomimetic Materials and Green Energy, Southern University of Science and Technology, Shenzhen 518055, China

Address correspondence to Yahui Xue, xueyh@sustech.edu.cn; Lishun Fu, lishun.fu@kuang-chi.com

Supporting information to https://doi.org/10.26599/NR.2026.94909286

The Supplementary Information includes:

I. Notes S1-S3

II. Figures S1-S20

III. Tables S1-S2

References

Supplementary Notes

Note S1: Preparation of AgNWs aqueous dispersion

The AgNWs were synthesized through the modify polyol method according to previous report. In brief, 0.255 g of $AgNO_3$ were added to 25 mL of EG and stirred until completely dissolved, resulting in solution A. In addition, 0.70 g of PVP were dissolved in another 15 mL of EG under vigorous stirring to create solution B. Afterwards, solution A were slowly dropwise added into solution B under stirring for 15 min. Finally, the obtained homogeneous mixtures were transferred

Just Accepted

into Teflon-lined stainless-steel autoclave and heated for 6 h at 160 ℃. After the solvothermal reaction, the received products were thoroughly washed with distilled water and ethanol for several times. The synthesized AgNWs were formulated into a 1 wt.% aqueous dispersion and were stored in the fridge for further use.

Note S2: Synthesis of $Ti_3C_2T_x$ MXene nanosheets

MXene nanosheets were prepared employing a modified etching route to extract the Al layers from MAX phase based on the previous report. Typically, 1.6 g of LiF was introduced into 20 mL of HCl aqueous solution (9 M) and stirred until dissolved at room temperature. Then, 1.0 g of Ti_3AlC_2 powder was incrementally added to the uniform LiF/HCl solution and the obtained mixture was stirred at 45 ℃ for 24 h. Afterwards, the resultant solution was washed with deionized water and centrifuged at 3500 rpm several times until the pH of supernatant was above 6. The resulting black sediments were redispersed in distilled water and subjected to ultrasonic treatment in an ice-water bath for 30 min followed by centrifugation at 3500 rpm for 1 h, and the collected supernatant was mono/few-layered MXene nanosheets aqueous dispersion.

Note S3: Measurements

Tensile stress-strain curves were obtained using a SANS CMT4014 universal testing machine equipped with a 100 N load cell, at a loading rate of 1 mm/min [33]. The samples were attached to a paper frame with a rectangular hole of sufficient length and width to accommodate the gauge length and sample width. The sample length, width, and gauge length for all samples were 12, 3, and 5 mm, respectively. This rigid frame served as a protective barrier to prevent damage to the sample during attachment to the testing apparatus. After attaching the sample, the two legs of the frame were cut to release the sample for tensile measurements. The mechanical properties and their standard deviations were determined by testing 5 sample strips which were from the same film and taking the statistical average of five measurements. For all samples, the statistics did not include measurement results for samples that fractured near the edge of the paper frame.

The scattering parameters were obtained from a Ceyear 3671D vector network analyzer. The transmission (T), reflection (R), and absorption (A) coefficients are calculated from the scattering parameters (S_{11} and S_{21}). The total EMI SE (SE_T), reflection loss efficiency (SE_R) and absorption

Just Accepted

loss efficiency (SE_A) are obtained through T, R and A according the following formulas.

$$R=|S_{11}|^2, T=|S_{21}|^2 \quad (1)$$

$$A=1-R-T \quad (2)$$

$$SE_R=-10\lg(1-R) \quad (3)$$

$$SE_A=-10\lg\left[\frac{T}{(1-R)}\right] \quad (4)$$

$$SE_T=SE_A+SE_R \quad (5)$$

To further assess the EMI shielding capability, SE/t is normalized to eliminate the effect of thickness. In addition, SSE/t was used to evaluate the lightweight characteristic of materials and was calculated by the following equation, where t (cm) represents the thickness and ρ ($g\cdot cm^{-3}$) denotes the density.

$$SE/t=SE/t \quad (6)$$

$$SSE/t=SE/\rho t \quad (7)$$

To evaluate the mechanical and environmental durability of the IMCA-10 film, repeated bending and aging tests were conducted, respectively. The bending test involved subjecting a film sample to 90° bending for 400 cycles. For aging tests, the films were exposed to either ambient (25 °C, 60% RH for 7 days) or elevated temperature/humidity (80 °C, 85% RH for 72 h) conditions.

In the Joule heating testing, a direct current (DC) regulated power supply was applied to provide various input voltages. The surface temperature changes and heat distributions were recorded with a FILR E60 infrared thermal imaging camera. The sample for Joule-heating is in a rectangular shape with a spanwise dimension of 20 mm ×5 mm.

The antibacterial property of the IMCA-10 film was evaluated using a standard plate colony counting method. Staphylococcus aureus (representative Gram-positive bacterium) and Escherichia coli (representative Gram-negative bacterium) were selected as model strains. Overnight cultures of both bacteria were harvested by centrifugation, washed twice with phosphate-buffered saline (PBS, pH 7.4), and resuspended in PBS to a final concentration of approximately 10^6 CFU/mL. IMCA-10 films were cut into 1.0 cm × 1.0 cm squares, UV-sterilized for 30 min, and placed in sterile 6-well plates. For the experimental group, each film was immersed in 5 mL of bacterial suspension. For the blank control group, 5 mL of bacterial suspension was incubated without any film (or with an equal volume of sterile PBS). All groups

Just Accepted

were incubated at 37 °C for 4 h in an orbital shaker at 150 rpm. After incubation, the films were removed. 1 mL of each bacterial suspension was immediately mixed with 1 mL of neutralizer solution (containing 0.5% Tween 80 and 0.3% soybean lecithin in PBS) and allowed to stand at room temperature for 10 min. The neutralized suspensions were then serially diluted with sterile PBS. 100 μL of appropriate dilutions was spread onto agar plates. Plates were incubated at 37 °C for 24 h, and colonies were counted using an automated colony counter. The antibacterial rate (Eanti) was calculated according to the following equation:

$$Eanti=(N-Ns)/N \quad (8)$$

where N is the average colony count from the blank control group and Ns is that from the IMCA-10 film group, both at the same dilution factor.

The electrical output performance of the IMCA-10 film-based TENG, including open-circuit voltage, short-circuit current, and transferred charge was accurately determined using a programmable Keithley 6517B electrometer. A LinMot E1100 linear motor was used to energize IMCA-10 film-based TENG. The TENG tests were conducted at a temperature of ~25 °C and a relative humidity of ~60% RH.

Just Accepted

Supplementary Figures

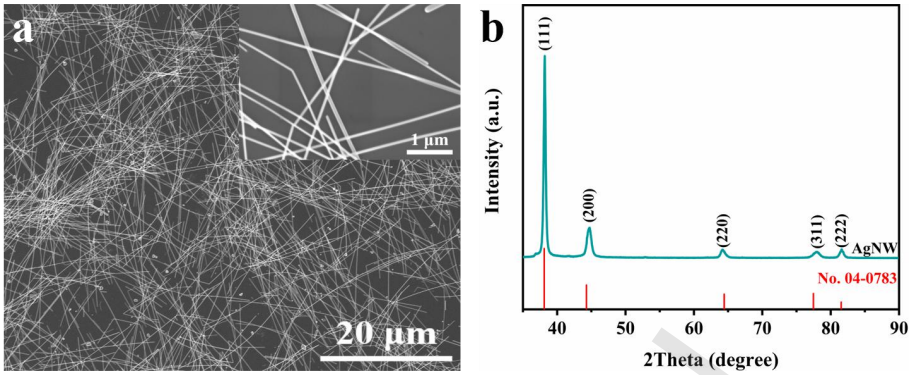


Fig. S1. (a) SEM images and (b) XRD pattern of the synthesized AgNW.

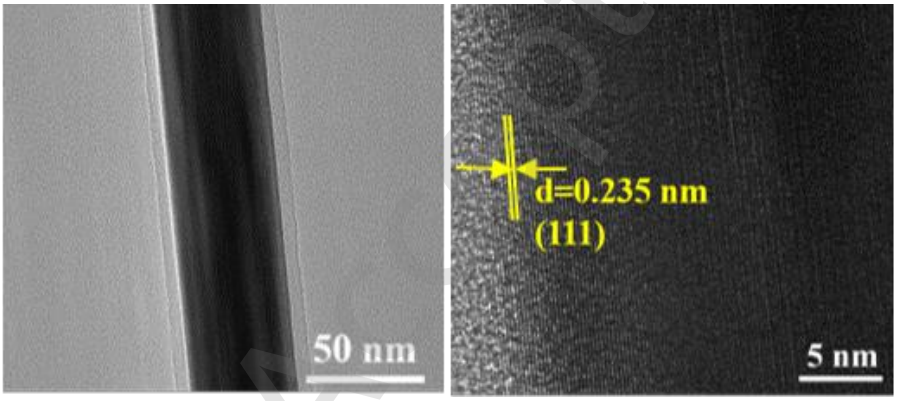


Fig. S2. TEM image and HRTEM image of the AgNW.

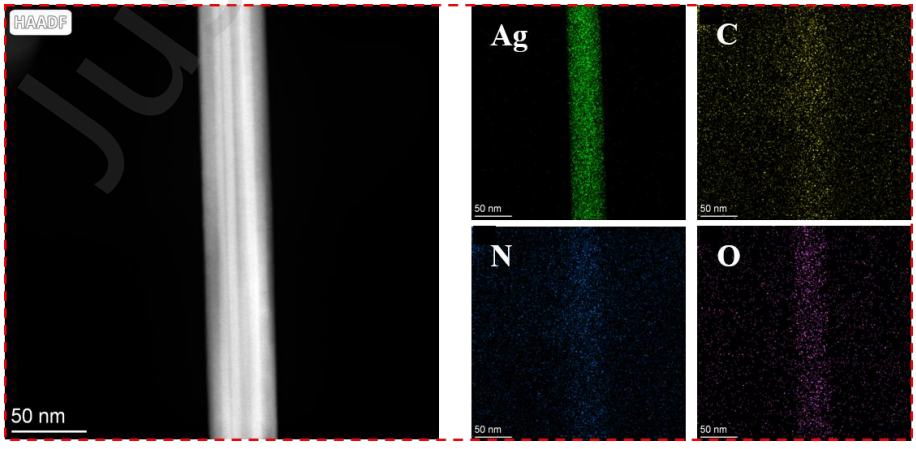


Fig. S3. HAADF-STEM image and corresponding elemental mapping images of the AgNW.

Just Accepted

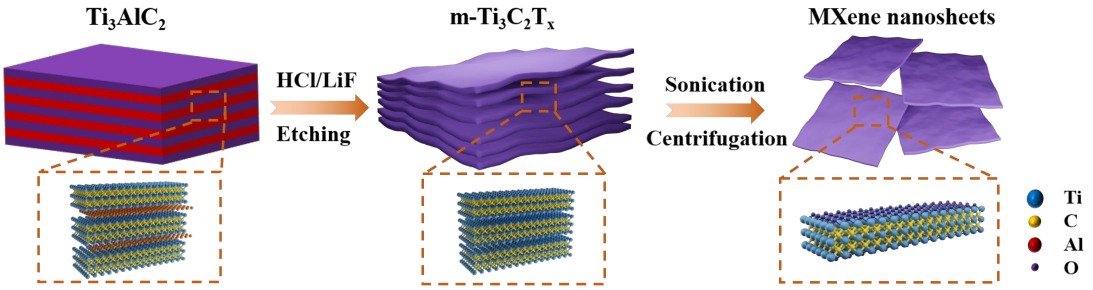


Fig. S4. The fabrication process of the MXene nanosheet.

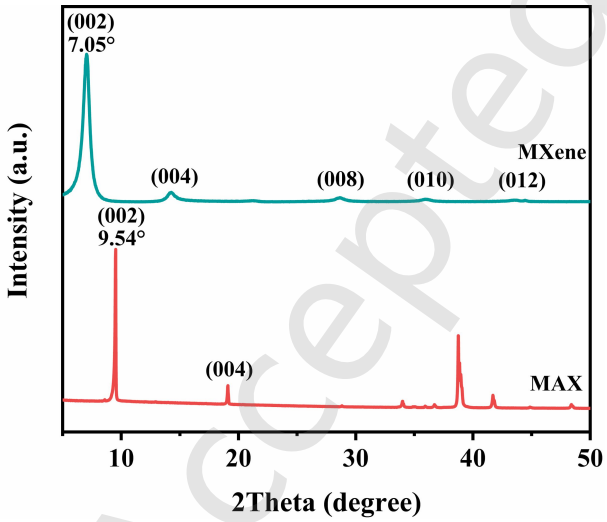


Fig. S5. XRD patterns of the MAX phase and MXene.



Fig. S6. Digital photo of the prepared MXene nanosheets dispersion: The Tyndall phenomenon.

Just Accepted

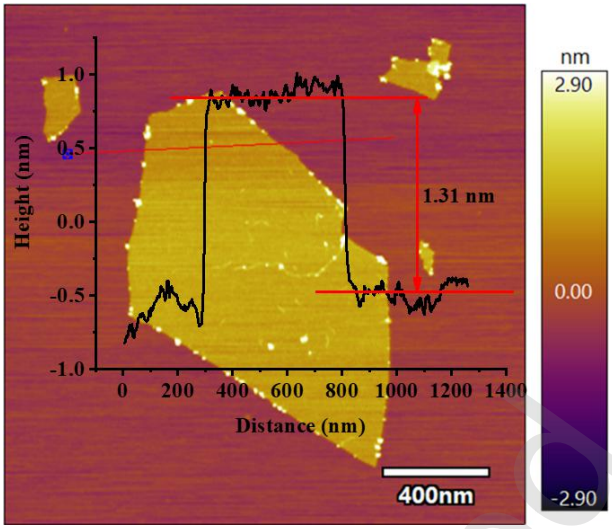


Fig. S7. AFM image of the MXene nanosheet.

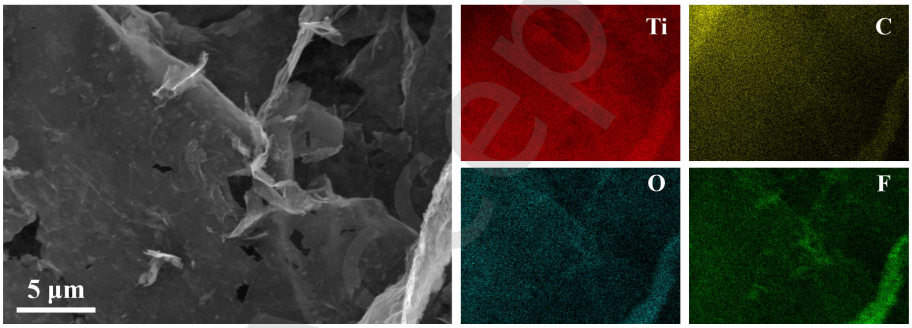


Fig. S8. ESD mapping images of the MXene nanosheet.

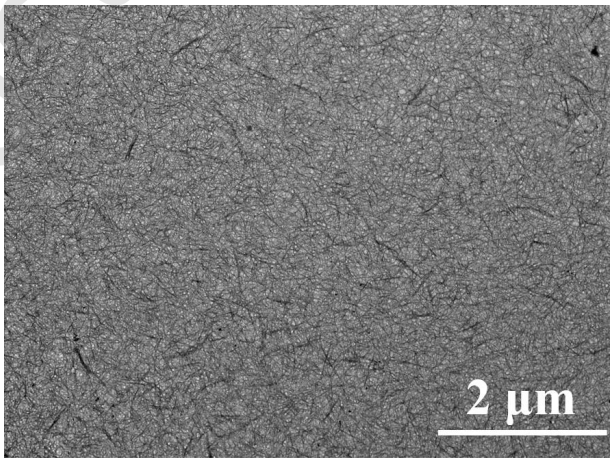


Fig. S9. TEM image of the CNF.

Just Accepted

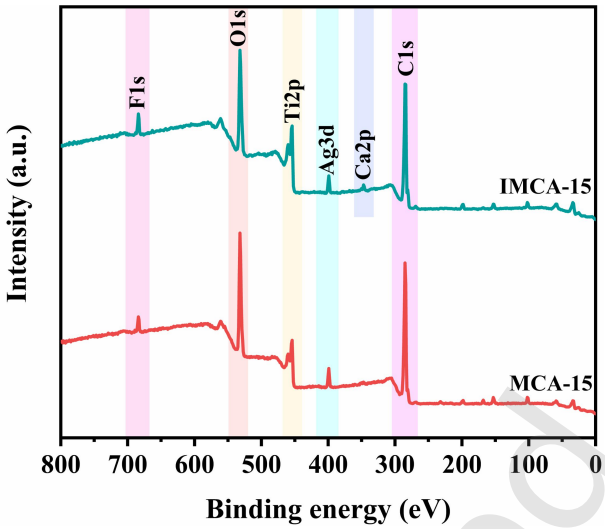


Fig. S10. XPS wide-scan spectra of the MCA-15 and IMCA-15 films.

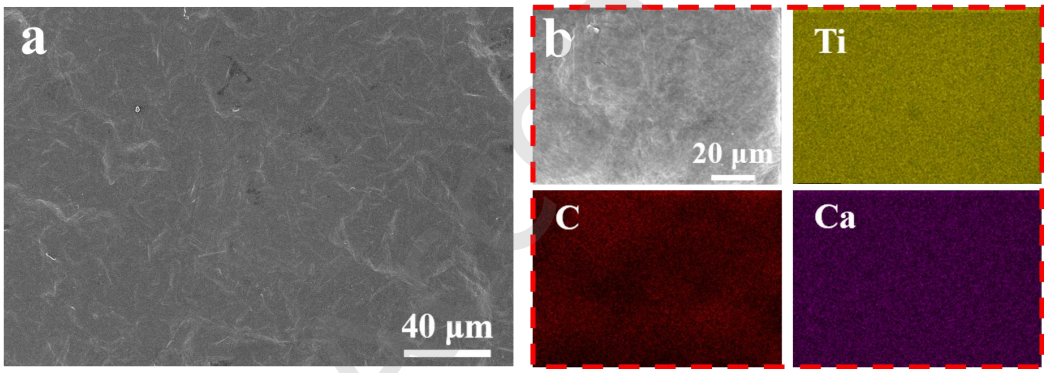


Fig. S11. (a) SEM image and (b) corresponding EDS mapping images of the surface of the IMCA-10 film.

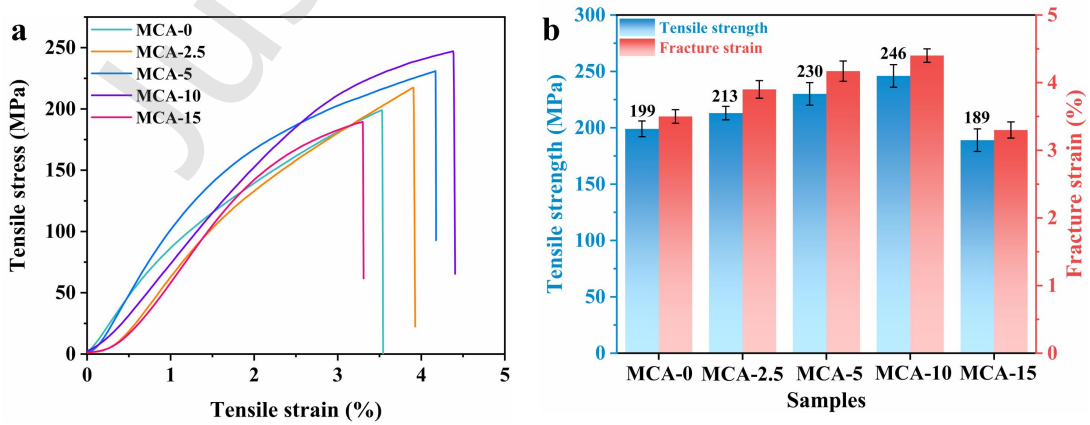


Fig. S12. Mechanical properties of the MCA-Y films. (a) Tensile stress-strain curves and (b) the corresponding tensile strength and breaking elongation of the MCA-Y films.

Just Accepted



Fig. S13. Photograph of an IMCA-10 film holding a 400 g weight.

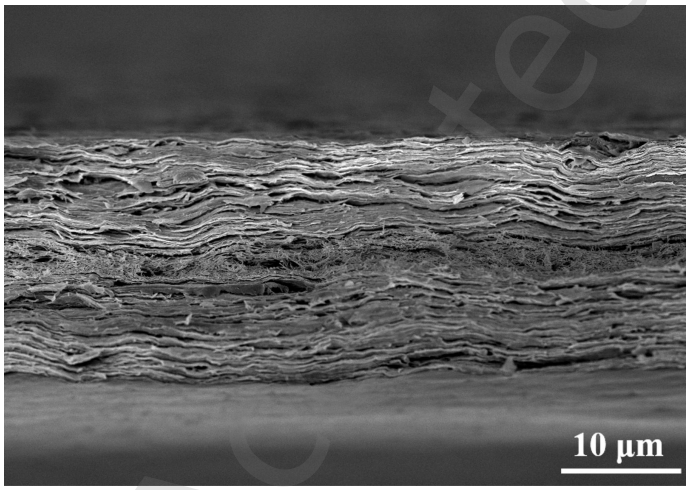


Fig. S14. SEM image of cross section of the IMCA-10 film after stretching.

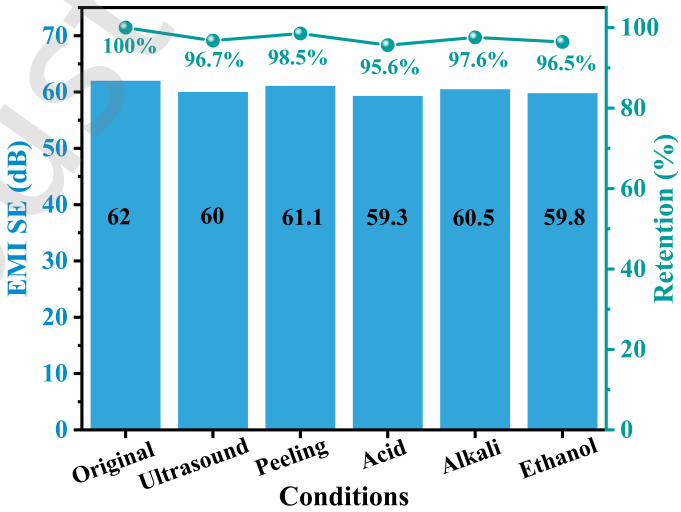


Fig. S15. Average SE_T and retention of the IMCA-10 film before and after exposure to different damages.

Just Accepted

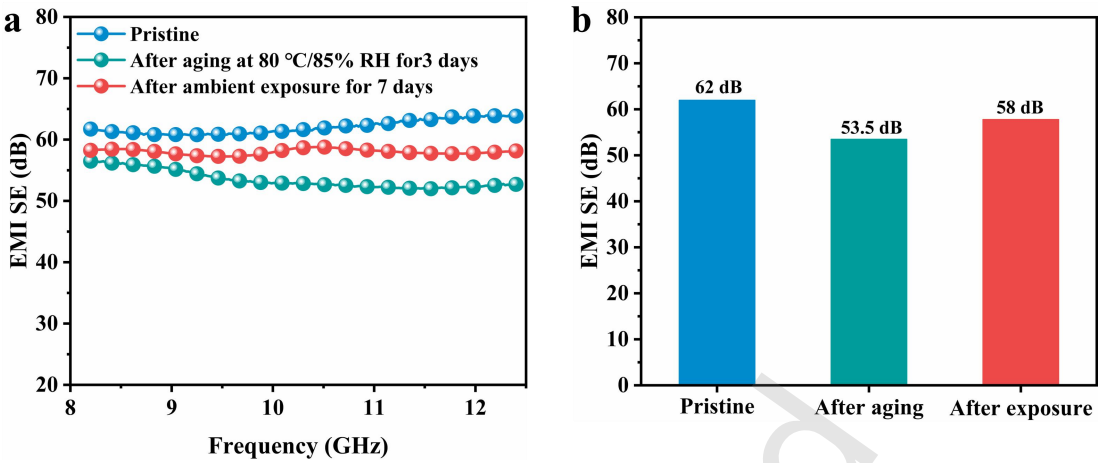


Fig. S16. EMI shielding performance of the IMCA-10 film before and after ambient oxidation exposure and hygrothermal aging tests: (a) EMI SE, and (b) EMI SE_T.

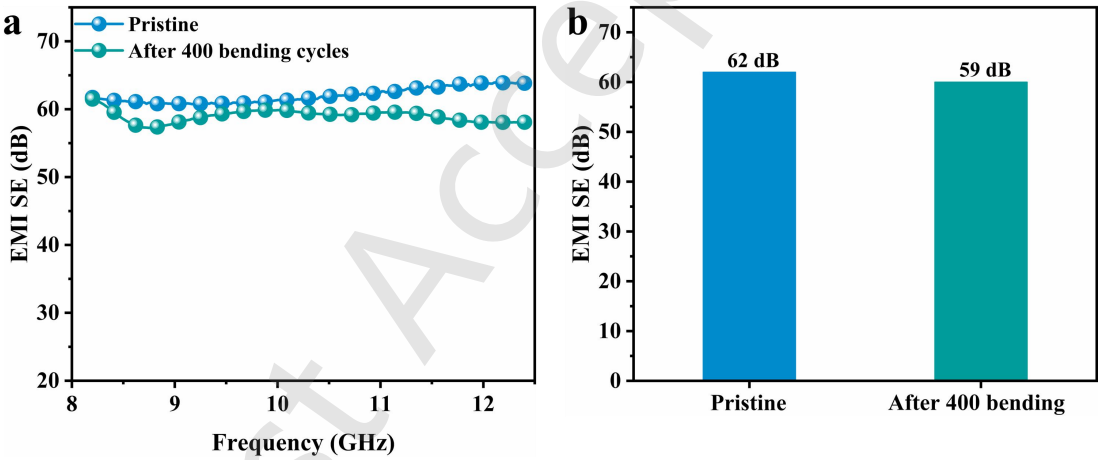


Fig. S17. EMI shielding performance of the IMCA-10 film before and after 400 bending cycles: (a) EMI SE, and (b) EMI SE_T.



Fig. S18. Photograph of wireless charging status of the mobile phone without shielding film.

Just Accepted

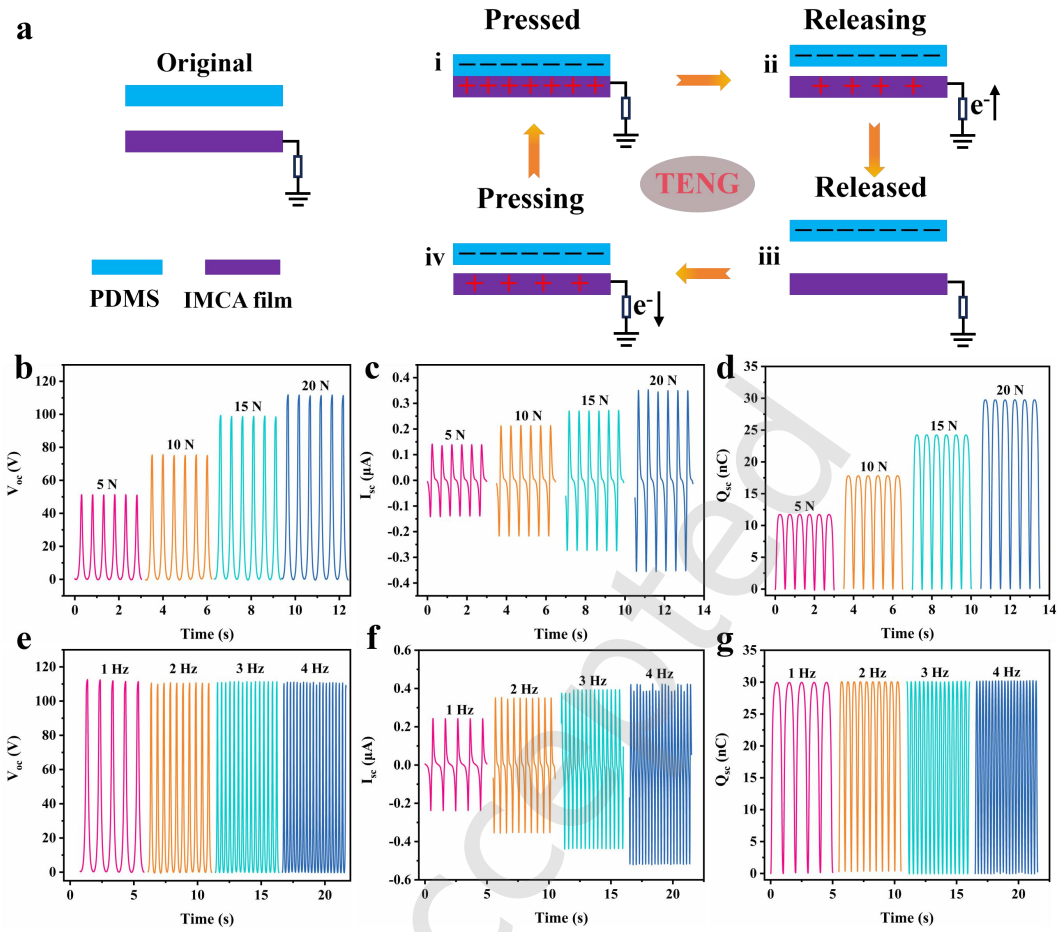


Fig. S19. The triboelectric performance of the IMCA-10 film-based TENG. (a) Structure and working mechanism of the IMCA-10 film-based TENG. The Voc (b), Isc (c) and Qsc (d) of the TENG under various pressures with a frequency of 2 Hz. The Voc (e), Isc (f) and Qsc (g) of the TENG under various frequencies with a pressure of 20 N.

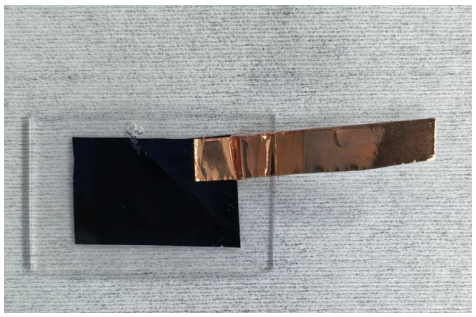


Fig. S20. Photograph of the wearable single electrode mode IMCA-10 film-based TENG device.

Just Accepted

Supplementary Tables

Table S1

Comparison of the EMI shielding performance of the IMCA-X composite films with other reported materials in thickness and EMI SSE/t.

Materials	EMI SSE/t ($dB \cdot cm^2 \cdot g^{-1}$)	Thickness (mm)	References
MXene/Cellulose	1326	0.167	[S1]
MXene/natural rubber	5693	0.066	[S2]
MXene/PC	6573.2	0.13	[S3]
MXene-SA-CNT	3087	3	[S4]
PVDF/MXene/AgNW	1091	0.6	[S5]
Graphene/PVDF	1265	0.1	[S6]
CNT/TX-100	5909	0.13	[S7]
Graphene/PEN	4278	0.048	[S8]
ANF/MXene/Liquid metal	6788	0.05	[S9]
Graphene/PEDOT: PSS	8040	1.5	[S10]
rGO/PDMS	5000	1	[S11]
MXene/PVA	3867	0.3	[S12]
CNF/MXene@Ga	6444.1	0.035	[S13]
MXene/PVA	9343	0.027	[S14]
MXene/ANF	8000	0.031	[S15]
CNF5@MXene-4	7029	0.035	[S16]
MXene/MMT-50	3254	0.045	[S17]
MOF/CNF/MXene	5000	0.2	[S18]
MXene/CB	8718	0.064	[S19]
CNT/WPU	459	0.4	[S20]
Ni/CF/PC	1376	0.31	[S21]
TPU/GNs/AgNW	6952	0.05	[S22]
MXene/PI	5865	0.38	[S23]
MOF/CNF/Graphene	5000	0.1	[S24]

Just Accepted

ANF/MXene/AgNW	5379.9	0.091	[S25]
Graphne/PI	1518	0.13	[S26]
PVA/MXene	4491	3.49	[S27]
MXene/PNF	8399	0.028	[S28]
ANF/AgNW/GNs	16545	0.04	[S29]
MXene/BC/Co@CNW	7649	0.043	[S30]
MXene/PEDOT: PSS/PBO	10143.4	0.025	[S31]
IMCA-15	16040	0.025	This work
IMCA-10	16550	0.023	This work
IMCA-5	15857	0.022	This work

Table S2

Comparison of EMI SE/t and tensile strength of the IMCA-X composite films with other reported materials.

Materials	**EMI SE/t (dB·cm^{-1})**	**Tensile strength (MPa)**	**References**
Bacterial cellulose/MXene	2770	126	[S32]
CNF/MXene/FeCo	1705	39	[S33]
CNF/MOF/MXene	6886	38	[S34]
MXenen/double-layered carbon	3641	8.9	[S35]
MXene/CNF	1325	12.7	[S36]
MXene/nanofiber	1231	35.1	[S37]
MXene/ANF	2733	70	[S38]
PI-MXene-MWCNT	8350	28.2	[S39]
Graphene/TPU	1333.3	58	[S40]
CNT/PEO/cellulose	2333.3	26.9	[S41]
CNT/GCC	15000	36.17	[S42]
BC/MXene/Liquid metal	13668	9.9	[S43]
CNT/BF/ANF	5126	20	[S44]
MOF/CNF/AgNW	6307	18	[S45]

Just Accepted

CMC/AgNW	14760	45	[S46]
MXene/PVA	8738	145.9	[S47]
MXene/ANF	10720	136.52	[S48]
CNF/MXene/Liquid metal	4059	36.12	[S49]
ANF/MXene/Liquid metal	4276	104	[S50]
ANF/MXene	7903	210	[S51]
ANF/MXene/Fe_3O_4	2776.7	70	[S52]
ANF@PPy/MXene	25250	17.5	[S53]
BC@PPy/MXene	8117.9	13.27	[S54]
(CNF/BN)-(CNF/MXene)	14615	73.5	[S55]
MXene/PNF	14583	125.1	[S56]
BNF/rGO/CNT/AgNP	5840	14.66	[S57]
Liquid metal/MXene/CNF	18571	10.5	[S58]
ANF/Liquid metal/ gelatin	4272	65.8	[S59]
Graphene/CNF/MOF	5050	46.33	[S60]
SNF@AgNP/MXene	10088	13	[S61]
MXene/BC/Fe_3O_4	1931	112	[S62]
ANF@PPy/MXene/AgNW	23400	52	[S63]
IMCA-15	26400	240	This work
IMCA-10	26956	315	This work
IMCA-5	26090	295	This work

Just Accepted

[S1] W. Cao, F. Chen, Y. Zhu, Y. Zhang, Y. Jiang, M. Ma, F. Chen, Binary strengthening and toughening of MXene/cellulose nanofiber composite paper with nacre-inspired structure and superior electromagnetic interference shielding properties, ACS Nano 12 (2018) 4583-4593.

[S2] W. Yang, J. Liu, L. Wang, W. Wang, A. Yuen, S. Peng, B. Yu, H. Lu, G. Yeoh, C. Wang, Multifunctional MXene/natural rubber composite films with exceptional flexibility and durability, Compos. B: Eng. 188 (2020) 107875.

[S3] R. Ding, H. Zheng, X. Zhao, F. Xue, P. Li, J. Xiong, Z. Chen, Z. Liu, Q. Peng, X. He, Skin inspired multifunctional crumpled $Ti_3C_2T_x$ MXene/tissue composite film, Compos. A:

Appl. Sci. Manuf. 158 (2022) 106967.

[S4] W. Wang, Z. Peng, Z. Ma, L. Zhang, X. Wang, Z. Xu, Y. Feng, C. Liu, D. Liang, Q. Li, High- efficiency electromagnetic interference shielding from highly aligned MXene porous composites via controlled directional freezing, ACS Appl. Mater. Interfaces 15 (2023) 47566-47576.

[S5] H. Cheng, Y. Pan, Q. Chen, R. Che, G. Zheng, C. Liu, C. Shen, X. Liu, Ultrathin flexible poly (vinylidene fluoride)/MXene/silver nanowire film with outstanding specific EMI shielding and high heat dissipation, Adv. Compos. Hybrid Mater. 4 (2021) 505-513.

[S6] B. Zhao, C. Zhao, R. Li, S. Hamidinejad, C. Park, Flexible, ultrathin, and high-efficiency electromagnetic shielding properties of poly (vinylidene fluoride)/carbon composite films, ACS Appl. Mater. Interfaces 9 (2017) 20873-20884.

[S7] S. Lu, J. Shao, K. Ma, D. Chen, X. Wang, L. Zhang, Q. Meng, J. Ma, Flexible, mechanically resilient carbon nanotube composite films for high-efficiency electromagnetic interference shielding, Carbon 136 (2018) 387-394.

[S8] S. Zhang, H. Sun, T. Lan, Z. Bai, X. Liu, Facile preparation of graphene film and sandwiched flexible poly (arylene ether nitrile)/graphene composite films with high EMI shielding efficiency, Compos. A: Appl. Sci. Manuf. 154 (2022) 106777.

[S9] M. Shen, X. Xu, J. Qi, X. Li, B. Xue, M. Zhu, Z. Zhang, X. Zheng, B. Li, Z. Shang, PMDI cross-linked rare earth/liquid metal reinforced ANF/MXene membranes for multifunctional electromagnetic interference shielding, Compos. A: Appl. Sci. Manuf. 182 (2024) 108178.

[S10] Y. Wu, Z. Wang, X. Liu, X. Shen, Q. Zheng, Q. Xue, J. Kim, Ultralight graphene foam/conductive polymer composites for exceptional electromagnetic interference shielding, ACS Appl. Mater. Interfaces 9 (2017) 9059-9069.

[S11] D. Ai, Y. Ma, H. Yu, Y. Chang, C. Wu, Y. Han, Y. Cheng, C. Dong, Lightweight graphene foam composites with enhanced electrical conductivity and microwave absorption for electromagnetic interference shielding, Mater. Res. Bull. 175 (2024) 112764.

[S12] H. Xu, X. Yin, X. Li, M. Li, S. Liang, L. Zhang, Lightweight $Ti_3C_2T_x$ MXene/poly (vinyl alcohol) composite foams for electromagnetic wave shielding with absorption-dominated feature, ACS Appl. Mater. Interfaces 11 (2019) 10198-10207.

Just Accepted

[S13] Y. He, J. Yang, W. Chen, W. Chen, L. Zhao, W. Qi, Gallium-doped MXene/cellulose nanofiber composite membranes with electro/photo thermal conversion property for high performance electromagnetic interference shielding, Chem. Eng. J. 464 (2023) 142565.

[S14] X. Jin, J. Wang, L. Dai, X. Liu, L. Li, Y. Yang, Y. Cao, W. Wang, H. Wu, S. Guo, Flame-retardant poly (vinyl alcohol)/MXene multilayered films with outstanding electromagnetic interference shielding and thermal conductive performances, Chem. Eng. J. 380 (2020) 122475.

[S15] J. Wang, X. Ma, J. Zhou, F. Du, C. Teng, Bioinspired, high-strength and flexible MXene/aramid fiber for electromagnetic interference shielding papers with Joule heating performance, ACS Nano 16 (2022) 6700-6711.

[S16] B. Zhou, Z. Zhang, Y. Li, G. Han, Y. Feng, B. Wang, D. Zhang, J. Ma, C. Liu, Flexible, robust, and multifunctional electromagnetic interference shielding film with alternating cellulose nanofiber and MXene layers, ACS Appl. Mater. Interfaces 12 (2020) 4895-4905.

[S17] L. Li, Y. Cao, X. Liu, J. Wang, Y. Yang, W. Wang, Multifunctional MXene-based fireproof electromagnetic shielding films with exceptional anisotropic heat dissipation capability and Joule heating performance, ACS Appl. Mater. Interfaces 12 (2020) 27350-27360.

[S18] T. Mai. W. Guo, P. Wang, L. Chen, M. Qi, Q. Liu, Y. Ding, M. Ma, Bilayer metal-organic frameworks/MXene/nanocellulose paper with electromagnetic double loss for absorption-dominated electromagnetic interference shielding, Chem. Eng. J. 464 (2023) 142517.

[S19] X. Fan, M. Li, X. Li, F. Ye, J. Xue, L. Zhang, L. Cheng, Electromagnetic interference shielding $Ti_3C_2T_x$-bonded carbon black films with enhanced absorption performance, Chin. Chem. Lett. 31 (2020) 1026-1029.

[S20] H. Li, D. Yuan, P. Li, C. He, High conductive and mechanical robust carbon nanotubes/waterborne polyurethane composite films for efficient electromagnetic interference shielding, Compos. A: Appl. Sci. Manuf. 121 (2019) 411-417.

[S21] D. Xing, L. Lu, K. Teh, Z. Wan, Y. Xie, Y. Tang, Highly flexible and ultra-thin Ni-plated carbon-fabric/polycarbonate film for enhanced electromagnetic interference shielding, Carbon 132 (2018) 32-41.

[S22] C. Wang, X. Chen, Y. Zhang, J. Chen, Y. Zhu, Enhanced electromagnetic interference

Just Accepted

shielding, thermal management, and Joule heating performance in polymer composite film by incorporating hybrid graphene-silver nanowire networks, Mater. Today Nano 29 (2025) 100583.

[S23] J. Chen, X. Hu, Z. Nie, Y. Feng, S. Qi, R. Wang, Flexible multilayer MXene/polyimide composite film with excellent electromagnetic interference shielding and photothermal conversion performance, J. Alloys Compd. 990 (2024) 174399.

[S24] M. Yuan, Y. Fei, H. Zhang, B. Qiu, L. Shen, X. He, M. Liang, S. Zhou, Y. Chen, H. Zou, Electromagnetic asymmetric films comprise metal organic frameworks derived porous carbon for absorption-dominated electromagnetic interference shielding, Compos. B: Eng. 233 (2022) 109622.

[S25] Z. Ma, S. Kang, J. Ma, L. Shao, Y. Zhang, C. Liu, A. Wei, X. Xiang, L. Wei, J. Gu, Ultraflexible and mechanically strong double-layered aramid nanofiber-$Ti_3C_2T_x$ MXene/silver nanowire nanocomposite papers for high-performance electromagnetic interference shielding, ACS Nano 14(7) (2020) 8368-8382.

[S26] V. Tran, D. Nguyen, A. Nguyen, M. Hofmann, Y. Hsieh, H. Kan, C. Hsu, Electromagnetic interference shielding by transparent graphene/nickel mesh films, ACS Applied Nano Mater. 3(8) (2020) 7474-7481.

[S27] Z. Guo, Y. Li, P. Jin, T. Zhang, Y. Zhao, Y. Ai, H. Xiu, Q. Zhang. Q. Fu, Poly (vinyl alcohol)/MXene biomimetic aerogels with tunable mechanical properties and electromagnetic interference shielding performance controlled by pore structure, Polymer, 230 (2021) 124101.

[S28] L. Wang, Z. Ma, Y. Zhang, H. Qiu, K. Ruan, J. Gu, Mechanically strong and folding-endurance $Ti_3C_2T_x$ MXene/PBO nanofiber films for efficient electromagnetic interference shielding and thermal management, Carbon Energy 4 (2022) 200-210.

[S29] D. Guo, Y. Huo, C. Mu, B. Wang, J. Xiang, A. Nie, K. Zhai, T. Xue, F. Wen, Z. Liu, Flexible aramid nanofiber/Ag nanowires/graphene nanosheets composite films with sandwich structure for high-performance electromagnetic interference shielding and Joule heating, J. Alloys Compd. 923 (2022) 166401.

[S30] Y. Zhang, X. Zuo, S. Zhang, Z. Ma, G. Zhang, Flexible multifunctional magnetic-conductive Janus nanocomposite films towards highly-efficient electromagnetic interference shielding and thermal management, Compos. Sci. Technol. 256 (2024) 110756.

[S31] H. Duan, C. Wang, Y. Yi, X. Mu, H. Ding, Z. Bi, Y. Hu, B. Yu, Scalable,

Just Accepted

mechanically-robust, fire-resistance MXene/PEDOT: PSS/PBO film for efficient electromagnetic interference shielding and Joule heating performance, Chem. Eng. J. 483 (2024) 149302.

[S32] S. Luo, Q. Li, Y. Xue, B. Zhou, Y. Feng, C. Liu, Reinforcing and toughening bacterial cellulose/MXene films assisted by interfacial multiple cross-linking for electromagnetic interference shielding and photothermal response, J. Colloid Interface Sci. 652 (2023) 1645-1652

[S33] M. Ma, W. Tao, X. Liao, S. Chen, Y. Shi, H. He, X. Wang, Cellulose nanofiber/MXene/FeCo composites with gradient structure for highly absorbed electromagnetic interference shielding, Chem. Eng. J. 452 (2023) 139471.

[S34] Z. Guo, Y. Zhao, P. Luo, J. Wang, L. Pei, H. Yu, P. Song, F. Ren, P. Ren, Asymmetric and mechanically enhanced MOF derived magnetic carbon-MXene/cellulose nanofiber films for electromagnetic interference shielding and electrothermal/photothermal conversion, Chem. Eng. J. 497 (2024) 155707.

[S35] B. Li, S. Luo, S. Anwer, C. Chan, K. Liao, Heterogeneous films form $Ti_3C_2T_x$ MXene and porous double-layered carbon nanosheets for high-performance electromagnetic interference shielding, Appl. Surf. Sci. 599 (2022) 153944.

[S36] L. Chen, T. Mai, X. Li, P. Wang, M. Qi, Q. Liu, Y. Ding, M. Ma, 3D printing of customizable and lightweight multilayer MXene/nanocellulose architectures for tunable electromagnetic interference shielding via direct ink writing, Chem. Eng. J. 476 (2023) 146652.

[S37] S. Hu, P. Han, C. Meng, Y. Yu, S. Han, H. Wang, G. Wei, Z. Gu, Flexible and ultrathin MXene/nanofiber composite films by self-stacking assembly for enhanced electromagnetic interference shielding performance, Appl. Surf. Sci. 654 (2024) 159506.

[S38] J. Kim, M. Vu, B. Seo, D. Mani, S. Anand, T. Jeong, S. Kim, Multilayered graphene fluoride and $Ti_3C_2T_x$ MXene-based aramid nanofiber films with excellent thermal conductivity and electromagnetic interference shielding performance, Colloids Surf: A 685 (2024) 133121.

[S39] W. Liang, J. Wu, S. Zhang, P. Zhao, X. Zuo, G. Wang, Construction of PI-MXene-MWCNT nanocomposite film integrating conductive gradient with sandwich structure for high-efficiency electromagnetic interference shielding in extreme environments, Carbon 228 (2024) 119328.

Just Accepted

[S40] B. Shen, Y. Li, D. Yi, W. Zhai, X. Wei, W. Zheng, Strong flexible polymer/graphene composite films with 3D saw-tooth folding for enhanced and tunable electromagnetic shielding, Carbon 113 (2017) 55-62.

[S41] L. Zhang, B. Yang, J. Teng, J. Lei, D. Yan, G. Zhong, Z. Li, Tunable electromagnetic interference shielding effectiveness via multilayer assembly of regenerated cellulose as a supporting substrate and carbon nanotubes/polymer as a functional layer, J. Mater. Chem. C 5 (2017) 3130-3138.

[S42] M. Yang, Q. Wei, J. Li, Y. Wang, H. Guo, L. Gao, L. Huang, X. He, Y. Li, Y. Yuan, Flexible composite carbon films prepared by a pancake-making method for electromagnetic interference shielding, Adv. Mater. Interfaces 7 (2020) 1901815.

[S43] M. Liu, H. Zhang, Z. Zhang, K. Zhang, Z. Chen, L. Pan, J. Zhou, Jujube-cake inspired lightweight and flexible MXene/liquid metal/bacterial cellulose electromagnetic interference shielding film with excellent Joule heating and thermal conductivity, Compos. Sci. Technol. 255 (2024) 110722.

[S44] S. Song, L. Li, D. Ji, J. Zhao, Q. Wu, Q. Wang, Flexible basalt fiber/aramid nanofiber/carbon nanotube electromagnetic shielding paper with outstanding environmental stability and Joule heating performance, ACS Appl. Mater. Interfaces 15 (2023) 35495-35506.

[S45] C. Liang, J. He, Y. Zhang, W. Zhang, C. Liu, X. Ma, Y. Liu, J. Gu, MOF-derived CoNi@C-silver nanowires/cellulose nanofiber composite papers with excellent thermal management capability for outstanding electromagnetic interference shielding, Compos. Sci. Technol. 224 (2022) 109445.

[S46] Y. Dai, N. Sun, D. Jiang, Z. Wang, Q. Ding, Z. Zhang, Y. Liu, Ultrathin and highly flexible layered silver nanowires/carboxymethyl cellulose nanofiber nanocomposite films for electromagnetic interference shielding, Int. J. Biol. Macromol. 278 (2024) 134770.

[S47] J. Dong, Z. Li, C. Liu, B. Zhou, C. Liu, Y. Feng, Highly oriented MXene/polyvinyl alcohol films prepared by scalable layer-by-layer blade coating for efficient electromagnetic interference shielding and infrared stealth, Nano Res. 17(6) (2024) 5651-5660.

[S48] J. Wang, T. Song, W. Ming, M. Yele, L. Chen, H. Zhang, X. Zhang, B. Liang, G. Wang, High MXene loading, nacre-inspired MXene/ANF electromagnetic interference shielding composite films with ultralong strain-to-failure and excellent Joule heating performance, Nano

Just Accepted

Res. 17(3) (2024) 2061-2069.

[S49] Y. He, J. Yang, W. Chen, W. Chen, L. Zhao, W. Qi, Gallium-doped MXene/cellulose nanofiber composite membranes with electro/photo thermal conversion property for high performance electromagnetic interference shielding, Chem. Eng. J. 464 (2023) 142565.

[S50] M. Shen, X. Xu, J. Qi, X. Li, B. Xue, M. Zhu, Z. Zhang, X. Zheng, B. Li, Z. Shang, PMDI cross-linked rare earth/liquid metal reinforced ANF/MXene membranes for multifunctional electromagnetic interference shielding, Compos. A: Appl. Sci. Manuf. 182 (2024) 108178.

[S51] J. Wang, X. Ma, J. Zhou, F. Du, C. Teng, Bioinspired, high-strength, and flexible MXene/aramid fiber for electromagnetic interference shielding papers with Joule heating performance, ACS Nano, 16 (2022) 6700-6711.

[S52] H. Zhang, J. Cheng, K. Liu, S. Jiang, J. Zhang, Q. Wang, C. Lan, H. Jia, Z. Li, Electric-magnetic dual-gradient structure design: Aramid nanofiber/MXene/Fe_3O_4 hybrid film for absorption-dominated electromagnetic interference shielding, J. Colloid Interface Sci. 678 (2025) 950-958.

[S53] M. Cheng, X. Xu, H. Zhang, S. Kong, Z. Feng, F. Meng, Y. Wang, Self-assembling, flexible and stable aramid nanofiber/polypyrrole/MXene composite film for efcient electromagnetic interference shielding, dual-driven heating and infrared thermal camouflage, Chem. Eng. J. 505 (2025) 159112.

[S54] Y. Yang, J. Tang, H. Guo, F. Pan, H. Jiang, Y. Wu, C. Chen, X. Li, B. Yuan, W. Lu, Robust and environmentally friendly MXene-based electronic skin enabling the three essential functions of natural skin: Perception, protection, and thermoregulation, Nano Lett. 24 (2024) 10883-10891.

[S55] L. Wang, L. Lang, X. Hu, T. Gao, M. He, H. Qiu, X. Ji, H. Guo, Y. Zhang, S. Huang, Multifunctional ionic bonding-strengthened ($Ti_3C_2T_x$ MXene/CNF)-(BNNS/CNF) composite films with Janus structure for outstanding electromagnetic interference shielding and thermal management, J. Mater. Sci. Technol. 224 (2025) 46-55.

[S56] L. Wang, Z. Ma, Y. Zhang, H. Qiu, K. Ruan, J. Gu. Mechanically strong and folding-endurance $Ti_3C_2T_x$ MXene/PBO nanofiber films for efficient electromagnetic interference shielding and thermal management. Carbon Energy 4(2) (2022) 200-210.

Just Accepted

[S57] L. Wang, D. Xu, J. Zhou, Multilayer composite films with enhanced electromagnetic interference shielding and thermal management properties based on bamboo cellulose nanofibers, Carbohydr. Polym. 354 (2025) 123309.

[S58] L. Ran, X. Ma, L. Qiu, F. Sun, L. Zhao, L. Yi, X. Ji, Liquid metal assisted fabrication of MXene-based films: Toward superior electromagnetic interference shielding and thermal management, J. Colloid Interface Sci. 652 (2023) 705-717.

[S59] Y. Zhu, K. Qian, M. Miao, X. Feng, Oxhide gelatin-regulated aramid nanofiber/liquid metal films with sandwiched structure for electromagnetic interference shielding, Int. J. Biol. Macromol. 276 (2024) 133897.

[S60] M. Yuan, Y. Fei, H. Zhang, B. Qiu, L. Shen, X. He, M. Liang, S. Zhou, Y. Chen, H. Zou, Electromagnetic asymmetric films comprise metal organic frameworks derived porous carbon for absorption-dominated electromagnetic interference shielding, Compos. B: Eng. 233 (2022) 109622.

[S61] N. Yi, C. Zhang, Z. Wang, Z. Zheng, J. Zhou, R. Shang, P. Zhou, C. Zheng, M. You, H. Chen, H. Cheng, M. Weng, Multi-functional $Ti_3C_2T_x$-silver@silk nanofiber composites with multi-dimensional heterogeneous structure for versatile wearable electronics, Adv. Funct. Mater. 35 (2024) 2412307.

[S62] M. Liu, H. Zhang, X. Huang, Z. Zhang, K. Zhang, Z. Chen, J. Zhou, L. Pan, An electric-magnetic dual-gradient composite film comprising MXene, hollow Fe_3O_4, and bacterial cellulose for high-performance EMI shielding and infrared camouflage, Adv. Funct. Mater. 35 (2025) 2419077.

[S63] G. Chu, Z. Nie, Y. Peng, H. Xu, X. Yang, X. Guo, M. Jiang, F. Dong, Z. Guo, S. Qi, J. Zhang, Spin-coating ANF based multilayer symmetric composite films for enhanced electromagnetic interference shielding and thermal management, J. Colloid Interface Sci. 679 (2025) 521-530.

Just Accepted